Russian Chemical Reviews **71** (7) 593 – 617 (2002) © 2002 Russian Academy of Sciences and Turpion Ltd

DOI 10.1070/RC2002v071n07ABEH000725

Modern applications of NMR tomography in physical chemistry. The characteristic features of the technique and its applications to studies of liquid-containing objects

I V Koptyug, R Z Sagdeev

Contents

I.	Introduction	593
II.	The nuclear magnetic resonance imaging technique	593
III.	Structure and properties of liquid-containing materials	599
IV.	NMR porosimetry	605
V.	Supplement	610

Abstract. This review concerns the state-of-the-art in the field of NMR tomography. The scope and limitations of the method, its capabilities, and some of the most widely used applications in physical chemistry are discussed. It is demonstrated that the technique is able to provide a vast variety of information about the state of objects under study and on the physicochemical processes occurring in them, which can be gained owing to the specific features of the technique. The review predominantly covers the studies of the structure and properties of various liquid-containing objects. The bibliography includes 232 references.

I. Introduction

Nuclear magnetic resonance tomography, or magnetic resonance imaging (MRI), has long been used in medical and biological research. Currently, this technique is being utilised for not only diagnosis of diseases but also operative control in clinical therapy and in studies of functional activity of the human brain. Recently, magnetic resonance imaging has also been used in studies of various objects of inanimate matter. Modern methods of multinuclear magnetic resonance allow one to image the internal structure of a vast variety of samples and to investigate the properties of and processes occurring in materials with a spatial resolution of the order of hundreds and even tens of micrometres.

Today, an extensive literature on the physicochemical applications of MRI has evolved, concerning a vast variety of applications. Therefore, the authors of this review tried to give the readers an idea of the most widespread avenues of applications of this technique and to present some appropriate illustrative examples. The choice of both applications and examples is to a great extent subjective. In most cases, it was dictated by authors' opinion about the importance of a particular application and by the field of research they are involved in.

There is also a number of objective factors that preclude unambiguous classification of particular experiments. For instance, any NMR experiment can in principle be carried out with spatial resolution, which leads to an almost infinite number of possible imaging experiments. This review leaves the communications concerned with obtaining spectral rather than spatial information as well as the NMR studies performed without spatial resolution out of consideration. The authors also leave aside specific biological and medical applications of this technique in spite of enormous literature in this field. It should be noted that there are no fundamental differences between particular experimental techniques employed in medical experiments and those used in physicochemical studies and that many physicochemical research strategies were initially developed for medical applications of MRI. A vast variety of processes occurring in living organisms, *e.g.*, pulsatory flow of liquids, gas diffusion in porous media, *etc.*, are also of considerable interest for chemists. At the same time, many experimental techniques employed in medical research have initially been tested and evaluated using model objects of inanimate matter. Therefore, it is impossible to leave biomedical applications of MRI out of consideration altogether.

Some features basically differentiate MRI from other modern methods of imaging the internal structure of various objects. Therefore, this review pays considerable attention to specific features of the technique, which is of great importance for assessing possible fields of its applications. The review mainly covers the publications concerned with the imaging and studies of the properties of liquid-containing objects.

I V Koptyug, R Z Sagdeev International Tomography Centre, Siberian Branch of the Russian Academy of Sciences, ul. Institutskaya 3A, 630090 Novosibirsk, Russian Federation. Fax (7-383) 233 13 99. Tel. (7-383) 233 35 61. E-mail: koptyug@tomo.nsc.ru (I V Koptyug) Tel. (7-383) 233 14 48. E-mail: itc@tomo.nsc.ru (R Z Sagdeev)

Received 4 April 2002
Uspekhi Khimii **71** (7) 672 – 699 (2002); translated by A M Raevsky

II. The nuclear magnetic resonance imaging technique

1. General remarks

Magnetic resonance imaging [1–4] undoubtedly owes its origin to the emergence and development (in the mid-1940s) of radiospectroscopy as a field of experimental science and first of all to successful pioneering ESR experiments by Zavoiskii [5] and studies on the observation of NMR signals in condensed matter carried out by the research groups headed by Bloch [6] and Purcell.[7] Studies of the spin echo carried out by Hahn [8] in the 1950s are also of great importance for the development of MRI, since recording the spin echo signals serves as the basis for many particular MRI techniques. In 1966, Ernst and Anderson [9] proposed a promising method of extracting spectral information using the Fourier transform. This was a breakthrough in the development of modern pulsed NMR [10–12] which is the basis of magnetic resonance imaging. Since the early 1970s, commercial NMR spectrometers have been equipped with computers for acquisition, processing and presentation of experimental data. Modern experi-

ments are so sophisticated and the amount of information is so large that computers are an integral part of NMR equipment. In 1971, Jeener† proposed the use of two-dimensional Fourier transform in NMR and thus laid the groundwork for multidimensional NMR spectroscopy.[13–16] In essence, magnetic resonance images represent a kind of multidimensional NMR spectra.[17] Moreover, both NMR spectroscopy and MRI can be considered as particular cases of multidimensional NMR experiments in a generalised space of coordinates, frequencies and time. In 1973, Lauterbur[18] reported the first tomographic image obtained using the ^{1}H NMR signals. Commercial NMR tomographs for medical research have been produced since the early 1980s. The mid-1980s were marked by the development of hardware, design of novel experimental techniques, which allowed considerable enhancement of spatial resolution and the emergence of NMR microtomography or magnetic resonance microimaging (MRM).

It should be noted that it is hard to discriminate between MRI and MRM.‡ Similarly to the commonly accepted term 'microscopy', a formal line between them can be drawn through a volume element of the order of $(0.1\ \text{mm})^3$, which represents the resolution limit for the naked eye.[19] Nevertheless, even such a conventional distinction is sometimes ambiguous, since the spatial resolution is often anisotropic. For instance, many experiments are performed with an in-plane resolution of tens of micrometres and a slice thickness of several millimetres.

2. Obtaining an image

The basis for nuclear magnetic resonance is the interaction between the nuclear spins and the static and alternating magnetic fields. In practice, a spin system usually represents an ensemble of nuclear spins which is described by the total magnetisation vector $\mathbf{M}$. At thermal equilibrium in a static magnetic field $\mathbf{B}_0$, the nuclear spins tend to line up with the field so that the vector $\mathbf{M}$ is directed along $\mathbf{B}_0$. Conventionally, the magnetic field is aligned along the z axis of the laboratory frame of reference, $\mathbf{B}_0 = \mathbf{B}_{0z}$. A 90° flip of the longitudinal magnetisation vector $\mathbf{M} = \mathbf{M}_z$ about the x axis creates the transverse magnetisation $\mathbf{M}_y \perp \mathbf{B}_0$. In pulsed NMR, the magnetisation vector is flipped by applying the radiofrequency (RF) pulses for which the magnetic field $\mathbf{B}_{1x}$ is perpendicular to the field $\mathbf{B}_0$ while the flip angle, α, depends on the amplitude of the field $\mathbf{B}_{1x}$ and the duration of the RF pulse. In particular, the pulse that flips the magnetisation vector 90° is called the 90°-pulse. After the flip, the transverse magnetisation vector experiences free precession about the $\mathbf{B}_{0z}$ direction and creates the observed signal at the resonance frequency ω equal to the spin precession frequency in the external field $\mathbf{B}_0$.

Precession of the transverse magnetisation vector is accompanied by its irreversible decay with the characteristic time T_2 as a result of transverse, or spin-spin, relaxation. Often, the actual decay time, T_2^*, of the observed signal is shorter than T_2 ($T_2^* < T_2$) owing to different spin precession frequencies that can be due to the differences in the local magnetic fields. For a system of immobile spins such a dephasing is reversible and the spin system can be rephased by reversal of the applied field gradient or by inversion of the phase of the spin precession by applying a 180°-pulse. Rephasing of the magnetisation leads to creation of the spin echo signal. In the case of NMR, the width of a spectral line is determined by the time T_2 (T_2^*). Return of the spin system to thermal equilibrium and recovery of the longitudinal magnetisation vector $\mathbf{M}_z \parallel \mathbf{B}_0$ is associated with the effect of the longitudinal, or spin-lattice, relaxation occurring with the characteristic time T_1. Knowledge of the relaxation times T_1, T_2, T_2^* and the relaxation time in the rotating frame of reference, $T_{1\rho}$, allows one to extract valuable information on the structure of and processes in the objects under study. Generally, the relaxation times depend on the magnitude of the applied magnetic field and the relaxation time measurements have been a routine procedure in the NMR experiments.[10–12]

The basics of MRI are very simple. The position of a single line in the NMR spectrum is determined by the resonance frequency, ω, which is to a first approximation proportional to the applied external magnetic field $\mathbf{B}_0$:

$$\omega = \gamma \mathbf{B}_0, \tag{1}$$

where γ is the gyromagnetic ratio of the nucleus under study with a nonzero spin. The NMR spectrum of water in two tubes placed in a uniform magnetic field (see Fig. 1) will exhibit a single, relatively narrow line (see Fig. 1 *a*) regardless of the amount of water in the tubes and their arrangement. However, if the magnetic field is nonuniform (*i.e.*, it is a function of the spatial coordinates), the resonance frequency also becomes a function of the spatial coordinates of the nuclear spin. Most of experiments are carried out using constant magnetic field gradient; in this case the magnitude of the magnetic field is a linear function of coordinate:

$$\mathbf{B}_z = \mathbf{B}_{0z} + \left(\frac{\mathrm{d}\mathbf{B}_z}{\mathrm{d}x}\right)x = \mathbf{B}_{0z} + \mathrm{G}_x x, \tag{2}$$

(here, the magnetic field gradient, G_x, is applied along the x axis). It should be emphasised that applying the G_x gradient does not change the orientation of the total magnetic field at any point of the sample along the z axis, while the magnetic field amplitude becomes a linear function of the coordinate x. Usually, the second term in expression (2) is smaller than the first one. The gradients G_y and G_z are defined analogously.

Thus, if two tubes shown in Fig. 1 are placed in a magnetic field given by expression (2), different locations of the tubes on the x axis denote that they experience different magnetic fields and, hence, give the NMR signals at different frequencies (Fig. 1 *b*). Moreover, inhomogeneity of the magnetic field within each tube leads to different resonance frequencies of microscopic volumes of

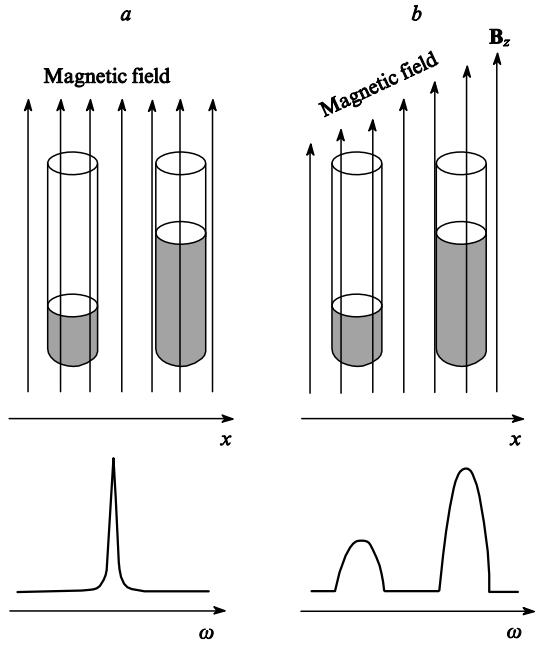


Figure 1. A schematic representation of the NMR spectrum of water in two tubes placed in the magnetic field $\mathbf{B}_z$.
Homogeneous magnetic field (*a*), magnetic field strength is a linear function of coordinate x (*b*).

† See J Jeener, in *Ampere International Summer School, Basko Polje, Yugoslavia, 1971*

‡ The term 'MRI' is mostly used in medical literature; however, many non-medical applications of the method cannot also be called 'microimaging'. Since in fact we deal with the same experimental method, in this review we prefer to use a more general term, 'MRI', while the term 'MRM' is used in those cases where high spatial resolution should be emphasised.

water at different coordinates x. It is easily seen that applying the G_x gradient allows one to obtain an integrated projection of the sample under study on the direction of the gradient vector.

The approach illustrated in Fig. 1 can be used in NMR spectroscopy for simultaneous analysis of several samples to increase the throughput of experimental technique, which is of particular importance in, *e.g.*, combinatorial chemistry.[20]

Even such a simple one-dimensional (1D) experiment allows the obtaining of useful information in studies of samples of appropriately chosen symmetry. For instance, by applying the field gradient along the axis of a cylindrical sample one can obtain the 1D profiles of the liquid content. Experiments with sequential recording of the 1D profiles in studies of the adsorption of water on a cylindrical bead pack of the adsorbent particles are illustrated in Fig. 2. The advantages of this technique are its simplicity and the possibility of fast recording the 1D profiles (data acquisition times are of the order of hundreds of microseconds), since in this case the signal is recorded after a single application of the pulse sequence. In the MRI studies the pulse sequence includes the RF pulses and pulsed magnetic field gradients G_i, which are applied between the RF pulses or simultaneously with them.

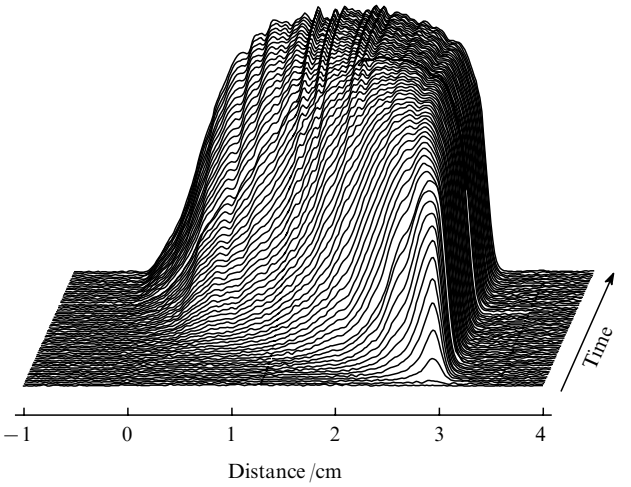


Figure 2. One-dimensional water distribution profiles in the axial direction of the cylindrical bead pack (internal cylinder diameter was 21 mm) comprised of small adsorbent granules (2–3 mm) recorded during the pumping of moist air through initially dry adsorbent.
Recording each profile took 260 s. A total of 64 profiles were collected within 4 h 40 min. Air flow direction from right to left.

Practical implementation of such a 1D experiment is based on recording the temporal evolution of the transverse magnetisation of the sample (in the form of the free induction decay or the spin, stimulated or gradient echo) in the presence of a field gradient. In this case, the spin precession frequencies are different during the acquisition time; therefore, this technique is called the frequency encoding of spatial information. The angle of rotation, or the phase, of the magnetisation vector precessing in the xy plane continuously changes during the signal acquisition time $0 \leqslant t \leqslant T_{\rm reg}$

$$\varphi = \omega t = \gamma \mathbf{B}_z t = \gamma \mathbf{B}_{0z} t + \gamma \mathrm{G}_x x t. \tag{3}$$

The MRI experiments can be conveniently described using the concept of the k-space. Let us define the components of the wave vector $\mathbf{k}$ as follows:

$$k_x = \frac{\gamma \mathrm{G}_x t}{2\pi}; \tag{4}$$

The components k_y and k_z are defined analogously. During the recording of a signal in the presence of the gradient G_x, the k_x value is continuously changed, so the detection process is equivalent to a discrete sampling of the NMR signal intensity at a discrete set of equidistant time or k_x values. Thus, in contrast to some other imaging techniques,[21] the MRI experiments involve scanning the space of the wave vector $\mathbf{k}$ rather than real space. Therefore, n-dimensional imaging of an object requires scanning the k-space of the same dimension n with the centre at $\mathbf{k} = 0$. Image reconstruction in the real coordinate space is possible using, *e.g.*, the n-dimensional Fourier transform

$$S(\mathbf{k}) = \int \rho(\mathbf{r}) \exp(i 2\pi \mathbf{k}\mathbf{r}) \mathrm{d}\mathbf{r}, \tag{5}$$

$$\rho(\mathbf{r}) = \int S(\mathbf{k}) \exp(-i 2\pi \mathbf{k}\mathbf{r}) \mathrm{d}\mathbf{k}, \tag{6}$$

where $S(\mathbf{k})$ is the experimental NMR signal recorded by scanning the k-space and $\rho(\mathbf{r})$ is the spin density. The $\rho(\mathbf{r})$ value is proportional to the concentration of the substance under study.

The frequency encoding of the NMR signal (see above) allows the recording of a line in the k-space, *e.g.*, a line along the k_x direction if $k_y = k_z = 0$. Obtaining a two-dimensional (2D) image in, *e.g.*, the xy plane requires additional recording of the NMR signal at those points of the k-space for which $k_y \neq 0$. To this end, a pulsed gradient G_y is applied to the transverse magnetisation before the beginning of signal acquisition. As a result, the spin system is displaced in the k-space along the k_y direction by an increment

$$k_y = \frac{\gamma \mathrm{G}_y \delta}{2\pi}, \tag{7}$$

where δ is the duration of the pulse gradient. Then, after recording the NMR signal in the presence of G_x, one gets a new line of points in the k-space, which is parallel to the preceding line. Multiple repetition of this procedure with step-by-step variation of the amplitude of the pulsed gradient G_y allows collecting the necessary 'two-dimensional' array of the signal amplitudes in the k-space. Since the pulsed gradient G_y is applied before recording the NMR signal, it changes the phases rather than the precession frequency of the magnetisation vectors contributing to the observed signal during the acquisition time. Therefore, this procedure is called the phase encoding of spatial information or signal.

A drawback of the phase encoding procedure is multiple repetition of experiments to obtain a complete set of k_y values. Prior to each repetition of the pulse sequence the spin system should return to thermal equilibrium. This takes time $T_{\rm r}$ of the order of $3T_1 - 5T_1$. For an analogue-to-digital converter with a maximum sampling rate of 1/(2.5 μs), recording a line of 128 points in the k-space takes 128×2.5 μs = 320 μs. Obtaining a two-dimensional image of size 128×128 pixels requires 128 lines in the k-space to be recorded. For instance, in the case of bulk water ($T_1 = 2.7$ s) it would take $128 \times 3 \times T_1 \approx 17$ min. This way of scanning the k-space is inefficient since only 0.004% of the total duration of experiments is spent for recording the NMR signal. In addition, an increase in the image dimension leads to reduction of the size of the volume elements contributing to each image pixel, which in turn reduces the signal-to-noise ratio. Therefore, signal averaging is required which even greater extends the duration of experiments.

A three-dimensional (3D) image can be obtained by recording the signals from a set of planes in the k-space, corresponding to different k_z values ($k_z = \gamma \mathrm{G}_z \delta / 2\pi$). This can be done using the phase encoding along the z axis, namely, the pulse sequence is augmented with the pulsed gradient G_z of duration δ. Clearly, such experiments take a very long time. Obtaining an image of size $128 \times 128 \times 128$ pixels requires 128×128 lines in the k-space to be recorded, which takes more than 36 h ($128 \times 128 \times 3 \times T_1$). However, an experiment with a sample with $T_1 = 10$ ms takes only

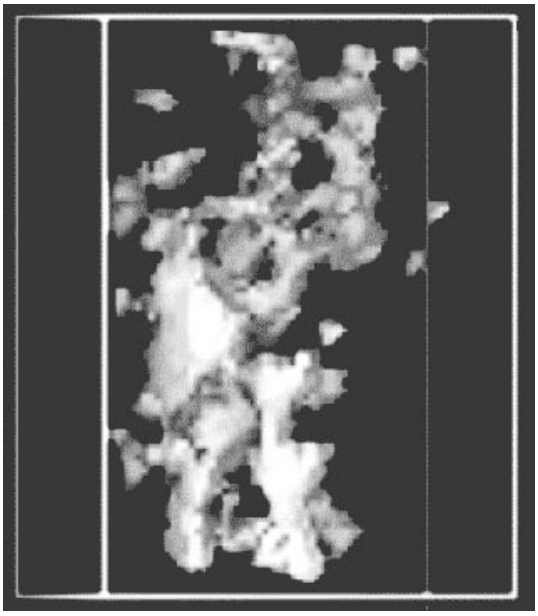


Figure 3. A reconstructed three-dimensional image of a cluster comprised of porous fine-grained (200 μm) alumina impregnated with Vaseline oil and filling out the interstices of a bead of large (5 mm) alumina granules. The latter contain no liquid and do not contribute to the NMR signal.

8 min. An example of a reconstructed three-dimensional image of an object is shown in Fig. 3.

Another approach to studies of three-dimensional objects involves recording two-dimensional images from one or several slices rather than the entire object (Fig. 4). Slice selection is most often achieved by using selective RF pulses. Any RF pulse has a limited excitation bandwidth, the bandshape being dependent on the parameters of the pulse. Many types of pulses nearly equally affect all spins in the frequency range $\omega_0 \pm \Delta\omega/2$ (ω_0 is the frequency of the RF pulse and $\Delta\omega$ is the bandwidth) while the spins with characteristic frequencies lying beyond this frequency range remain nearly unaffected. The $\Delta\omega$ value is inversely proportional to the duration of the RF pulse; therefore, a relatively long RF pulse range has a narrow excitation bandwidth. In the case of homogeneous magnetic field this can be used for, *e.g.*, selection of a particular signal in the entire NMR spectrum and obtaining a spatially resolved image for one of the components of a mixture. If the selective pulse is applied simultaneously with the field gradient G_z, this pulse becomes spatially selective and affects only those spins within a slice perpendicular to the axis along which the gradient is applied. As mentioned above, the time of the two-dimensional experiments is mainly spent for the recovery of the equilibrium magnetisation. Since selective pulses have no effect on the magnetisation outside the selected slice, one can scan lines in the *k*-space, corresponding to other slices of the sample while the magnetisation within a given layer relaxes to the equilibrium value. This allows imaging of a number of slices that do not intersect within the sample instead of one slice nearly without extension of the duration of the experiments. Since the directions of the gradients G_x, G_y and G_z are mutually orthogonal, the use of their linear combinations makes it possible to select a slice with arbitrary spatial orientation and to carry out a two-dimensional scan of a slice in the *k*-space without physical rotation of the sample. To obtain an excitation pattern with steeper transition regions at the edges of a slice, the so-called shaped RF pulses are employed.[22–25]

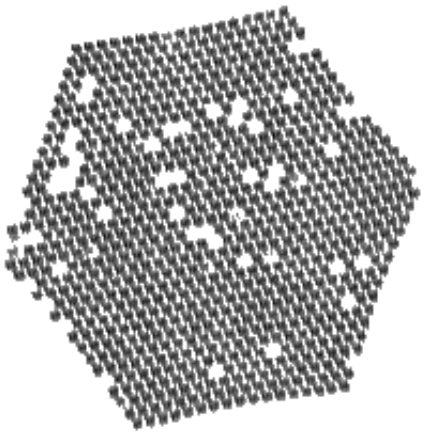


Figure 4. Two-dimensional image of a slice of a glass capillary-bundle column saturated with water.
The nominal in-plane spatial resolution was 5×5 μm^2 at a slice thickness of 15 mm. The diameter of individual capillaries was 40 μm. White spots in the image correspond to the blocked capillaries containing no water.

Practical implementation of the frequency encoding of an NMR signal involves application of the gradient echo or a combination of the gradient echo and the spin echo. In the former case, rephasing of the spin precession is achieved by reversal of the gradients in the pulse sequence, while in the latter case this is achieved by rephasing using a 180° pulse. In contrast to the gradient echo, the spin echo also eliminates the effects caused by internal field gradients, differences in chemical shifts and heteronuclear spin-spin interaction.

In recording the echo signal an important parameter is the echo time T_e, *i.e.*, the effective time of the evolution of the transverse magnetisation, which is equal to the time interval between the instants of creation and rephasing of the transverse magnetisation and corresponds to the maximum spin echo signal. Often, the relaxation time of the transverse magnetisation, T_2, is shorter than the shortest achievable T_e value. This leads to considerable loss of sensitivity of the experimental technique. The effective time of the transverse relaxation, T_2^*, of samples with large internal magnetic field gradients can be shorter than T_2. In the latter case, it is more appropriate to use the spin echo technique, since the spin echo amplitude decays with the characteristic time T_2, while the gradient echo signal decays with the time constant T_2^*. If T_2 is much shorter than the shortest achievable T_e, in some cases the free induction decay in the presence of the external field gradient is recorded instead of the echo signal, which corresponds to radial trajectories in the *k*-space. Subsequent image reconstruction can be performed by either interpolation of the signal at the nodes of a rectangular grid followed by multidimensional Fourier transformation [26] or from projections.[27,28] A number of experimental techniques,[29] *e.g.*, single point imaging (SPI) [30,31] and single point ramped imaging with T_1 enhancement (SPRITE) [32–35] are based exclusively on the phase encoding (no frequency encoding is used).

Generally, the imaging time depends on the image dimension, imaging procedure, sensitivity, relaxation times of the nuclear spins used for recording the NMR signal and is to a great extent determined by the desired spatial resolution. Shortening the duration of the experiments is particularly important when dealing with fast dynamic processes. There is a number of approaches that were used as the basis for creation of fast imaging techniques for obtaining two- and three-dimensional NMR images.[36–39] These techniques employ shortening the recovery time between the repetitions of the pulse sequences, recording more than one line in the *k*-space during each application of the pulse sequence, optimisation of the trajectories in the *k*-space, *etc.* For instance, each repetition of the pulse sequence in fast procedures based on acquisition of the gradient echo signal [40] uses only a small part of the longitudinal magnetisation of the sample due to the applica-

tion of the RF pulse with a small flip angle, $\alpha \ll 90^\circ$. As a result, the spin system is not fully saturated and there is no complete NMR signal loss even if the recovery time T_r is much shorter than T_1. Yet another approach involves acquisition of a large set of the echo signals, each of them being corresponded to a different line in the k-space, during a single application of the pulse sequence.[41–43] Recently, considerable attention has been given to spiral rather than linear scan of the k-space.[44–46]

Magnetic resonance imaging can be used for mapping the RF field [47] and the static magnetic field [48–50] within the sample giving the NMR signal. Therefore, shimming the magnetic field in the NMR experiments is now transformed from a kind of art [51] into a field of exact science. This feature is used in MRI experiments for visualisation of the electromagnetic fields of the gradient coils and the fields created by eddy currents upon switching the external field gradients.[52–54] Visualisation of the electric fields in a sample is used for the determination of the densities of the electric currents flowing within the sample.[55–57]

Summing up, it should be mentioned that MRI experiments can be carried out using the gradients of the RF field B_1 (the so-called B_1-imaging) [58–61] instead of the gradients of the static field B_0. The advantage of this technique is its insensitivity to internal inhomogeneities of the static magnetic field. One can use the RF field gradients to obtain images as well as to determine the relaxation times, diffusion coefficients and flow rates of fluids.[62, 63]

3. Spatial resolution of MRI method

Magnetic resonance imaging is characterised by a relatively low spatial resolution. Experiments with a resolution of the order of $(5\ \mu m)^3$ should be considered exceptions. In most cases, a spatial resolution is of the order of tens and even hundreds of micrometres. Often, the slice thickness ($\sim 1-10$ mm) in two-dimensional NMR imaging studies exceeds the in-plane spatial resolution. It should be noted that the experimentally achievable spatial resolution is not the major advantage of the MRI technique.

The spatial resolution that can be achieved in the experiment depends on several factors. In many instances, the major contribution comes from the relatively low sensitivity of NMR. Often, almost no information can be extracted from an image obtained with high (nominal) spatial resolution because of the noisiness of the image. This is due to the fact that enhancement of spatial resolution is associated with a decrease in the size of the volume element of the image (voxel), which in turn causes a proportional reduction of the signal-to-noise ratio for each image pixel.[1] This ratio can be improved by accumulating the NMR signal by means of multiple repetition of the experiments; however, the duration of the experiments becomes unacceptably long.

Another factor responsible for the spatial resolution is the spectral width of the NMR signal used in the imaging experiments. As mentioned above, the NMR images can be treated as multidimensional NMR spectra, namely, as the dependences of the signal amplitude on one or a number of frequency coordinates. The nominal resolution equals the actual one if two neighbouring pixels of an NMR image correspond to two non-overlapped spectral peaks, *i.e.*, if the NMR signal is narrower than the frequency difference between the centres of the neighbouring image pixels. In principle, this limitation can be surmounted by increasing the amplitude of the field gradient whereby the image is stretched in the frequency coordinates. In practice, the field gradient amplitudes are limited by the operating range of experimental equipment ($100-1000$ G cm^{-1}). Increasing the field gradient amplitudes is a challenge to MRI studies of solids,[27, 64–69] since the width of the NMR signals of solids (up to hundreds of kilohertz) much exceeds the values typical of liquids. Therefore, MRI studies of solids are often carried out using the field gradients of the order of 10^4 G cm^{-1}.

It should be emphasised that limitations associated with the linewidth of the NMR spectra are characteristic of the frequency rather than phase encoding of the NMR signal. In addition, phase encoding excludes the appearance of artifacts in the NMR image originated from inhomogeneity of the magnetic field and differences in the chemical shifts.[29]

Yet another factor that limits the spatial resolution is displacement of the nuclear spins in space (including molecular diffusion) during the acquisition time. The self-diffusion coefficient, D, of bulk water at 20 °C is 2.0 cm^2 s^{-1}. If the acquisition time of one echo signal, T_{reg}, is 1 ms, the characteristic displacement of water molecules along the direction of the magnetic field gradient is $(2DT_{reg})^{1/2} \approx 2$ μm. If the diffusion motion of the molecules is restrained, the diffusion-controlled resolution limit can be in principle reduced. In the case of motion of macroscopic parts of the object under study one should use another time scale and consider the motion (displacement) during a much longer time interval, that is, the acquisition time of the entire NMR image rather than the acquisition time of one echo signal. In particular, displacement of the entire object (*e.g.*, a patient undergoing an MRI evaluation) during the time interval needed to perform all measurements should not be larger than the desired spatial resolution. In the case of periodic motions of the object under study (cardiac muscle contractions, pulsatory blood flow, *etc.*), imaging is often controlled by the period of the motion (*e.g.*, synchronisation with the electrocardiogram signal).

Currently, there has been intensive research aimed at enhancing the spatial resolution of the MRI technique.[70] An avenue of biomedical research is based on the possibility of using MRM with a spatial resolution of the order of 1 μm in studies of plant cells and in animal experiments. Miniaturisation of the receiver RF coils allows improvement of the signal-to-noise ratio. However, further enhancement of spatial resolution using this approach faces severe difficulties. Much more promising seem to be other strategies (in particular, the use of magnetic resonance force microscopy which combines NMR imaging and atomic force microscopy).[71–74]

4. Specific features, advantages and drawbacks of MRI techniques

An unquestionable advantage of MRI is the possibility of non-destructive (non-invasive) investigation of the internal structure and properties of various (including opaque) objects, which is of particular importance in medical research. Another advantage of the method is the lack of preferential direction, which allows obtaining spatial information along any direction or simultaneously along the three spatial coordinates.

Magnetic resonance imaging requires no probes or molecular tracers to be introduced into the object under study. Here, the nuclear spins of the molecules constituting the object under study are employed as inherent tracers. In principle, any nucleus with nonzero spin can give an NMR signal. The prospects for the MRI applications of a particular nucleus are first of all determined by the sensitivity of this nucleus and by the characteristic relaxation times. In practice, the number of different nuclei used in MRI experiments is limited and most of studies utilise the ^{1}H NMR signals.

In addition, in the case of multicomponent systems combining the NMR spectroscopy and MRI allow one to obtain separate images for each type of molecules or even each group of atomic nuclei in the molecules. Both approaches can also be used to obtain spatially resolved NMR spectra including those of a preselected volume element of arbitrary shape inside the sample (localised spectroscopy).[75–79] The capabilities of spatially localised MRI are illustrated in Fig. 5.

As mentioned above, the major drawback of MRI consists in relatively low spatial resolution. Besides, NMR in general and MRI in particular can be used to study a large number but not all kinds of materials. Operation with electromagnetic radiation in RF range ($100-1000$ MHz) imposes severe restrictions on the possibilities of studying metals and other conducting materials, since in this frequency range the skin layer is thin and the RF



Figure 5. An image of the logo of the International Tomography Centre of the Siberian Branch, Russian Academy of Sciences.
The image was obtained by spatial selection of the NMR signal using a simple 10-mm cylindrical tube filled with water as the sample.

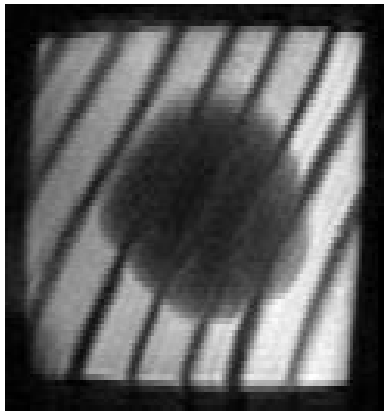


Figure 6. Image of a pine bar of a square cross section of $(1.7\ \text{cm})^2$ and 5 cm in height. The bar was initially frozen and was melting during the MRI experiments.
The two-dimensional image was obtained in the horizontal plane without slice selection. Brighter gradations of gray correspond to more intense NMR signal. The early and late zones of the growth rings are clearly visualised as bright and dark stripes, respectively. The dark spot at the centre of the image corresponds to the frozen liquid.

radiation does not penetrate into the interior of the entire sample. Placing a conducting object into a RF coil causes a considerable loss of the energy stored in the resonant circuit, which reduces its Q-factor and affects the sensitivity of the method employed. In addition, MRI utilises pulsed magnetic field gradients which induce eddy currents responsible for the loss of signal and image distortion in studies of conducting materials. Dielectric losses in samples with high dielectric constant also reduce the Q-factor of the RF circuit. Investigations of magnetic materials in static magnetic fields of strength less than 20 T are also impossible.

Often, some limitations are also imposed on the size of sample under study. Magnetic resonance microimaging allows one to achieve the highest spatial resolution and the signal-to-noise ratio; however, the size of the sample usually does not exceed several centimetres. Using biomedical MRI instruments, one can investigate objects of size from $\sim$10 cm up to a human body size. Currently, devices with open configuration are finding increasing application. They allow studies of objects of any size; this is achieved by moving the object under study or the device itself. In medicine, this type of systems is used for, *e.g.*, visualisation of internal organs during surgical operations [80, 81] and diagnosis.[82] The NMR logging systems, a 'hydroscope' device designed for the exploration and characterisation of the underground pools of water and other fluids (see below), a GARField device [83] for laboratory investigations of samples tens or hundreds of micrometres thick and the 'NMR Mouse', or a mobile explorer of the near-surface regions of large objects [84] can serve as examples of open design applications in other fields.

5. Image contrast mechanisms and informativity of the method

All things being equal, an n-fold increase in the spin density (concentration of the nuclear spins) causes an n-fold increase in the amplitude of the NMR signal. However, it is not necessarily true that if two signal amplitudes differ by a factor of n, the corresponding spin densities also exhibit the n-fold difference. This is due to the fact that the signal amplitude is a complex function of many parameters and first of all the spin relaxation times T_1 and T_2. As a result, in practice the value $\rho(\mathbf{r})F(P)$ is measured instead of the spin density $\rho(\mathbf{r})$ [see expression (6)]. The function F determines the degree of image contrast due to parameters P that are different from $\rho(\mathbf{r})$. Therefore, sometimes quantitative MRM measurements of the spatial distribution of, *e.g.*, water in an object under study are difficult or even impossible since the influence of other factors on the NMR signal cannot be avoided completely. It is this apparent disadvantage that makes magnetic resonance imaging a powerful tool which is much more versatile compared to other modern spatial imaging methods.[21]

Spin density measurements (by, *e.g.*, integrating signals in an NMR spectrum) provide no way for discriminating the liquid and frozen water. However, the relaxation times of water in the liquid and solid state are appreciably different, which creates a contrast in the NMR image of an object containing water in different states of aggregation (Fig. 6). The molecular spin relaxation times are rather sensitive to the environment, which allows this feature to be used in medical diagnosis. Often, pathological changes in tissues have virtually no effect on the spin density; however, they affect the T_1 and T_2 values, which leads to changes in contrast of corresponding regions in the NMR image. Sometimes contrast between the healthy and malignant tissues can be improved by introducing a contrast agent, *i.e.*, a paramagnetic compound that is capable of changing the relaxation times of the spin systems of water or lipids in tissues. The relaxation times are also sensitive to the concentration of oxygen, which allows studies of, *e.g.*, the dynamics of changes in the oxygen concentration in blood and tissues. In particular, this is used for visualisation of the brain regions responding to a particular external stimulus (functional MRI).[85]

A broad spectrum of applications of NMR imaging is to a great extent due to the fact that the nature of contrast of the NMR image depends on the experimental conditions and can be chosen by researches in a targeted manner depending on particular problems. For instance, by shortening the time delay between repetitions of the pulse sequence one can obtain NMR images with T_1-contrast — $\rho(\mathbf{r})F(T_1)$, — *i.e.*, the images in which the colour of a particular pixel characterises not only the local concentration of the resonance spins, but also their local spin-lattice relaxation time. This is due to the fact that the amplitude of the NMR signal of the nuclear spins with $T_1 \ll T_r$, which have time to return to thermal equilibrium during the time interval between successive repetitions of the pulse sequence, is maximum and independent of T_r, whereas the NMR signal of the spins with $T_1 \geqslant T_r$ is partially suppressed and its amplitude is a function of the T_1/T_r ratio. This is the case of the so-called T_1-weighted image.

Clearly, by varying the image contrast in a targeted manner one can obtain information not only on the time T_1 but also many other parameters characterising the spin system. However, the relaxation times (T_1, T_2, T_2^*, $T_{1\rho}$) occupy a special position among all these parameters. Nuclear spin relaxation is due to the fluctuating local magnetic interactions of the nuclear spins with their environment. The efficiency of the nuclear spin relaxation depends on the frequency spectrum corresponding to a particular type of interactions. The spectrum is to a great extent determined by both the motion of the probe molecule (and its fragments) and the motions of the molecular environment. The relaxation time T_1

is sensitive to components of the motion occurring at frequencies of the order of hundreds of megahertz, whereas the times T_2 and $T_{1\rho}$ are sensitive to the motions occurring in the kilohertz range. Therefore, by measuring the relaxation times one can study the frequency spectra of the molecular and atomic group motions and determine the correlation times and activation energies of such motions as well as particular distances in the system under study at the molecular level.

In addition to the spin density and relaxation times, the chemical shift, local magnetic fields, spin polarisation and spin-spin interactions can be used as the basis for image contrast in MRI studies. These parameters are sensitive to many physico-chemical properties of objects under study (*e.g.*, temperature, viscosity, mechanical stress, diamagnetic susceptibility, *etc.*) and processes occurring in them (*e.g.*, interaction with the surface, chemical transformations, flow and other types of motion, ordering, filler distribution, cross-linking, vulcanisation, ageing of materials, *etc.*). Experiments are designed in such a way that the changes in a property (process) of interest be responsible for changes in a certain spin-system parameter related to changes in a particular parameter of the measured NMR signal (resonance frequencies, amplitude, linewidth or phase).

Thus, virtually any property (process) influencing a certain parameter of the NMR signal can provide image contrast in the NMR imaging experiments. This allows both qualitative and quantitative studies of the spatial distribution of a particular property of the object at hand. Since the NMR signal is sensitive to some properties (processes), often the major problem is to separate the contributions of the process under study or the property of the object to this signal. Often, creation of the pulse sequences for MRI experiments and interpretation of the results obtained are substantially simplified when using a modular approach. In this case, the pulse sequence is augmented with a module responsible for creation of a particular type of contrast, which is executed before the module designed for collecting spatial information.

III. Structure and properties of liquid-containing materials

1. General remarks

Magnetic resonance imaging studies of liquid-containing solid porous materials allow one to elucidate their structure and properties as well as the distribution of the fluid within the pore space without performing solid-state NMR experiments.

The amplitude of the NMR signal of an image pixel characterises the pore volume filled with the liquid within the corresponding volume element. If the size of the liquid-filled pores exceeds the spatial resolution of the experimental method (> 10 μm), NMR imaging permits investigations of the morphology of porous materials. For instance, the pore size in most of rocks can be as large as 200 μm and even greater (in limestone rocks).[86] For smaller pores, each pixel of an NMR image corresponds to the NMR signal averaged over the particular volume element of the sample. If the pore size is much smaller than the spatial resolution, each image pixel characterises the local porosity of the sample and the presence of large non-porous inclusions and voids. If the pore size is comparable with the spatial resolution, the partial volume effects become of great importance for correct interpretation of experimental data.

As mentioned above, the amplitude of the NMR signal depends not only on the spin density (amount of liquid in the volume element) but also on some other parameters. By appropriately choosing the mechanism of image contrast formation one can obtain the distribution maps of various characteristics of the objects under study after processing the experimental data. Very often, investigations into porous materials involve mapping the nuclear spin relaxation times (T_1, $T_{1\rho}$, T_2, T_2^*). Relaxation-weighted NMR images are useful in revealing inhomogeneities of the properties of a porous medium,[87] while quantitative relaxation time measurements allow one to determine the permeability,[88] wettability, pore saturation levels,[89] pore size and many other characteristics. Quantitative distribution maps of these parameters can be derived from the relaxation time distribution maps using appropriate models. Spatial inhomogeneity of a sample can be quantified by constructing histograms and evaluating the nonzero distribution moments for the maps obtained as well as by calculating the spatial correlation functions of the measured parameters.[86]

Usually, the spin relaxation times of the liquids filling the pore system are shorter than those of bulk liquids. Because of the shortening of the time T_2 the amplitude of the NMR signal in the magnetic resonance images is often out of proportion to the content of the liquid (spin density) in a porous sample. Therefore, quantitative information is often extracted from a set of NMR images characterised by different degree of relaxation weighting. Computer simulation of the relaxation curves for each image pixel can then be used for deriving separate spin density and relaxation time maps.[86,90]

In practice, studies of systems containing a number of immiscible and miscible liquids are not infrequent. For instance, the distribution of water and hydrocarbons in rocks is of considerable interest for the gas and petroleum extraction industry, while the reagent-to-product ratio is an important parameter in studies of chemical reactions. In the case of multicomponent systems selective NMR imaging is possible. This can be achieved using a number of methods. If the NMR signals of the liquids differ in chemical shifts, selective pulsed excitation of a particular line in the NMR spectrum allows one to carry out imaging studies using the signal of this spectral line (chemical shift selective imaging, CSSI).[91,92] Selective pulses can also be used to suppress (saturate) all spectral lines except for that involved in the imaging procedure.[91] However, it should be noted that shortening of the spin relaxation times can lead to appreciable line broadening in the NMR spectra of the liquids in the pores (up to hundreds of Hz and more), which precludes separation of the contributions of particular spectral lines to the NMR signal based on differences in chemical shifts.[86]

Another approach is based on recording the free induction decay or the spin echo signal in the absence of external field gradients, which preserves the spectral information (chemical shift imaging, CSI).[93–95] Having aimed at extracting spatial information, in this case one should reject the frequency encoding of the NMR signal. Low-resolution spectral information can also be obtained using the phase encoding of the signal. In such a case it is convenient to reconstruct spectral information by, *e.g.*, simulating the temporal evolution of the signal by the sum of several exponentially decaying sine curves rather than using the Fourier transformation.[96]

If resonances are overlapped, chemical shift selective NMR imaging is impossible. In this case one should use distinctions between other parameters of the NMR signal. The contributions of different components of the system under study can be separated using differences in the spin relaxation times.[97–99] For instance, by choosing an appropriate echo time, T_e, one can observe the contribution of the liquid characterised by the longest time T_2. If the times T_1 differ appreciably, the pulse sequence can be augmented with an inversion pulse and a time delay that are applied prior to image readout. The time delay is chosen in such a way that the signal be recorded at a time instant corresponding to zero magnetisation of a particular liquid in a binary mixture during the spin-lattice relaxation process.[92,100] Collecting a set of images with different degree of relaxation weighting followed by computer simulation of the relaxation curves for each image pixel allows one to obtain separate relaxation time and spin density maps. If the relaxation times of the liquids in the mixture are substantially different, this feature can be used to obtain the separate spin density maps for the individual components of the mixture.[101] Scalar interactions occurring between inequivalent nuclei can also be used for separation of the contributions of

different liquids to the NMR signal by, *e.g.*, creating and detecting two-quantum coherence.[97, 102]

Doping water with paramagnetic ions makes it possible to 'hide' its NMR signal owing to the short T_2 time. This can be used for selective observation of the NMR signal of a hydrocarbon in pores containing both liquids.[103]

Yet another experimental technique involves the use of different magnetic nuclei [104] and their isotopes. For instance, saturation of porous rocks with D_2O/hydrocarbon or H_2O/fluorocarbon mixtures allows selective acquisition of the signal of a particular liquid.[94, 103] The possibility of recording NMR signals from other nuclei extends the range of useful chemical substances.

Porous materials are characterised by the presence of numerous interfaces between phases with substantially different magnetic susceptibilities. Placing samples of porous materials in a strong magnetic field of the NMR spectrometer produces large field gradients near the interfaces. In this case, the decay time of the transverse magnetisation, T_2^*, becomes much shorter than the spin-spin relaxation time, T_2. The reasons are the dephasing of the spin precession since all spins experience different magnetic fields and incoherence of the spin motion (owing to, *e.g.*, diffusion) in non-uniform magnetic field. As a result, gradient echo imaging allows better visualisation of structural defects. The NMR images obtained by the spin echo technique often exhibit artifacts in the form of bright spots near structural defects (due to difference in magnetic susceptibilities).[105] On the other hand, for many systems with T_2^* values in the submillisecond range, the gradient-echo technique produces no NMR signals at all. To prevent substantial shortening of the time T_2^*, experiments are usually carried out in relatively low fields and/or using multiple rephasing of the magnetisation by applying the sequence of 180° pulses [10] (the so-called Carr – Purcell – Meiboom – Gill, or CPMG, pulse sequence). It should be noted that the magnitudes of local field gradients allow assessment of the pore shape and evaluation of the pore sizes.[106] Using the relaxation time of the transverse magnetisation of a system of immobile spins, one can extract information on the distribution of the square of the strength of local field gradients, which serves as a measure of the difference between the actual pore shape and an ellipsoid.[107] The values obtained from comparison of the calculated and experimental parameters can serve as semiempirical characteristics of the pore space (in particular, the shape and size of pores and inter-pore channels).

In addition to the aforesaid, diffusion in external field gradients applied to encode spatial information also causes shortening of the time T_2^*. Obtaining high spatial resolution requires application of large external gradients; however, this can be accompanied by substantial shortening of the times T_2^*. When studying samples with the T_2 (T_2^*) values lying in the sub-millisecond range it is appropriate to use experimental methods based on the phase encoding of spatial information (SPI, SPRITE) [30 – 35] or on recording and collecting the free induction decay signals followed by image reconstruction from projections.[27] The relaxation times can also depend on the mechanical prehistory of the sample.[108]

Magnetic resonance imaging studies should be carried out taking into account specific features of systems of different nature. For instance, in most of biological objects the spin systems do not exhibit a single-exponential relaxation due to structural inhomogeneity at the cell and tissue level.[109] Plant tissues are saturated with air bubbles; therefore, the magnetic field can be strongly inhomogeneous. Some liquid-containing porous materials (*e.g.*, rocks) possess electrical conductivity. This reduces the signal-to-noise ratio as a result of reduction of the Q-factor of the resonant RF circuit, changes its resonance frequency and can lead to a limited penetration depth of the RF field into the sample due to the skin effect.[86] In this case, experiments are carried out in relatively weak magnetic fields (*i.e.*, at lower frequencies). Rocks and synthetic porous materials can contain paramagnetic impurities that are responsible for appreciable shortening of the T_2 times of liquids in pores, which can result in partial or complete loss of the NMR signal.

2. Model and synthetic porous materials

The internal structure of catalyst granules determines their efficiency in heterogeneous catalysis, service life and other properties. Rigby [110] has reported a more accurate structural representation of a porous medium (catalyst granules) which was based on complementary information obtained from the results of NMR imaging experiments (visualisation of the pores of size greater than 10 μm) and low-temperature nitrogen adsorption (pores of size less than 10 μm) and mercury porosimetry measurements. Then, he modelled the void space of a porous solid by separate representations of both the macroscopic and mesoscopic length scale properties of the material.[110] Nuclear magnetic resonance images (more correctly, spin density maps) of fluid-saturated solid granules can be used for determination of the local concentration of the fluid, *i.e.*, inhomogeneity of the sample porosity. The NMR images of alumina spheres saturated with an ethanol – water mixture revealed [111] a uniform structure with spherically layered solid material and voids, which is consistent with the manufacturing process of these particles. The spin density and T_1 time distributions of water in alumina were mapped.[112]

The T_1 maps allow one to reveal spatial inhomogeneities of the pore size distribution, while the effective diffusivity maps show inhomogeneities of the transport properties.[113] Experiments with water-saturated alumina and silica granules showed that these types of inhomogeneities are not necessarily correlated.[114, 115] Mention may be made that the case in point is structural inhomogeneities with a characteristic size exceeding the spatial resolution of the experimental technique. Microscopic structural inhomogeneities are averaged in the imaging experiments. It should be noted that if for porosity there is a simple statistical averaging, the dynamic averaging of the T_1 and diffusivity values is nontrivial. Gladden *et al.*[116] proposed quantitative characterisation of the sample inhomogeneity in terms of a fractal dimension of two-dimensional NMR images of the sample. Water-saturated cylindrical alumina granules placed in a tube filled with D_2O exhibited different effective diffusivity and, hence, tortuosity of the pore space in the radial and axial directions. This is in agreement with different fractal dimensions of the two-dimensional NMR images of the same granules, whereas the fractal dimensions of two-dimensional T_1 maps obtained in the axial and radial directions were identical.

Different diffusivity measurement techniques are 'sensitive' to the structure of the pore space at different length scales. An assumption was made [117] that the ratio of the pore space tortuosity determined in the experiments with H_2O/D_2O exchange to the tortuosity determined from the pulsed field gradient studies [8, 25, 118, 119] provides an estimate of the tortuosity associated with the sample inhomogeneity at a length scale of the order of the sample size. This assumption was confirmed by calculations of the tortuosity coefficient carried out with construction of the pore space grid using the NMR images of water-saturated porous granules. This allowed one to represent the tortuosity coefficient of the pore space as product of several tortuosity coefficients obtained for different length scales. Based on these concepts, an attempt has been undertaken at constructing a correct model of a porous medium taking into account the structural hierarchy, that is, the micro(meso)scopic and macroscopic length scales.[120] A mathematical model for prediction of the properties of porous media at the micro(meso)scopic length scale was constructed using information on porosity and the average pore size obtained from conventional porosimetry measurements. Reliability of the model constructed at the length scale less than 10 μm was evaluated by comparing the calculated and experimental T_1 values of water filling the pores. The model for description of the macroscopic structure at the length scale spanning the range from 40 μm (typical spatial resolution of NMR images) to the size of the object (several millimetres) was constructed in such a

way that the fractal dimensions of the calculated two-dimensional NMR images (and/or T_1 maps) be in agreement with the experimental fractal dimensions. A complete hierarchical model was validated by comparing the calculated and experimental values of the effective diffusivities and pore space tortuosity coefficients.

A study of a porous Pyrex glass filter containing cyclohexane (average pore diameter was 160 μm) has been reported.[121] The 1D NMR profiles obtained with a spatial resolution of 26 μm exhibited rather large signal amplitude fluctuations indicating some structural disorder at this length scale. From the distances between the neighbouring amplitude peaks one can extract statistically averaged information on the pore size and inter-pore distances. Both statistical analysis of the distribution histogram of the distances between the neighbouring peaks and calculations gave close values of the estimates of the average inter-pore distance. At distances from zero to 2–4 mm, the spatial correlation function of the signal amplitude fluctuations has a constant value while it rapidly decreases at longer distances. The results obtained are in good agreement with the data of the scanning electron microscopy (SEM) studies which, in contrast to MRI experiments, require a labour-consuming pre-treatment of the sample.

Signal amplitude fluctuations can also be due to a low signal-to-noise ratio. Lengthening the signal accumulation time allows the defects in a water-saturated, disk-shaped porous glass sample to be identified with ease.[105] If the in-plane spatial resolution is comparable with the average pore size, it is convenient to use thick-slice NMR imaging of the samples of relatively low porosity. At higher in-plane resolution, the best image contrast is achieved in the experiments carried out with the same resolution along the three spatial dimensions. The NMR images of different disk-shaped samples (average pore size varied from 5 to 200 μm) obtained with an isotropic spatial resolution of 100 μm exhibited only minor distinctions. Experiments revealed shortening of the relaxation times of water filling the pores of sizes 5 to 200 μm with a decrease in the pore size.[105] Magnetic resonance images of water in a glass bead pack have also been obtained.[122] Studies of porous systems in packed bed reactors by MRI technique have been reported.[123]

To determine the fractal properties of porous systems, two-dimensional and three-dimensional model porous structures obtained by computer simulation were fabricated on polystyrene layers using a plotter to construct two-dimensional or three-dimensional percolation clusters. Three-dimensional objects were composed as stacks of two-dimensional layers. Then water was allowed to fill the clusters to visualise the pore space. The measured fractal dimension was found to be in good agreement with that of the model. Based on the possibility of distinguishing the liquid in motion and at rest [25, 124–127] when analysing the flow pattern along the percolation cluster, the dead ends were excluded from consideration and the fractal dimension of the percolation backbone was determined. For model objects, this parameter was found to be lower than that of the entire cluster dimension. Experiments with natural porous systems (natural sponge, pumice stone, quartz sand and glass bead agglomeration) showed that the pore space is much more highly interconnected and the backbone can hardly be distinguished from the total pore space in terms of the fractal dimension.[128]

Relaxation times of the fluids contacting solid surfaces are strongly dependent on the surface properties. In particular, the relaxation times of fluid filling the pore system are shortened in the presence of paramagnetic atoms or molecules adsorbed on the surface. Catalyst poisoning with weakly paramagnetic coke formed in the pore space can change the relaxation times of fluids and cause partial blocking of pores. This feature was used for obtaining the NMR profiles of macroscopic distributions of coke formed in the reaction of ethanol dehydrogenation in alumina pellets.[129] After reduction of conversion degree to a particular value in the range from 100% to 50% the alumina pellets were removed from the reactor and saturated with water. MRI-studies revealed high inhomogeneity of coke formation in the pellets and strong dependence of coke profiles on the pellet position in the reactor. Analogous studies of zeolite HY were carried out using 2,3-dimethylpentane or xenon as the probe molecules.[130] Contacting coke causes a change in the chemical shift of xenon. Relaxation time measurements of 2,3-dimethylpentane showed an inhomogeneous composition of coke within the sample.

Diamagnetic adsorbates can also change the relaxation times of the fluids filling the pore system due to, *e.g.*, steric shielding of paramagnetic ions adsorbed on the pore walls from the fluid molecules.[131] For instance, adsorption of platinum hexachloride ($PtCl_6^{2-}$) on the developed surface of a porous support causes an increase in the nuclear spin relaxation times of protons of the liquids that fill the pore space of the support.[131, 132] This fact was used [132] for determining the type of macroscopic spatial distribution of the active component over the surface of the support, which is an important characteristic of supported catalysts. Experiments were carried out using γ-Al_2O_3 pellets with different types of spatial distribution of platinum hexachloride. The NMR images confirmed good agreement between the T_1 maps of the fluids filling the pore space and the platinum distribution profiles obtained using conventional visualisation techniques. Magnetic resonance microimaging studies allowed the real-time redistribution dynamics of adsorbed platinum hexachloride to be traced for the first time during competing adsorption of $PtCl_6^{2-}$ and oxalic acid from solution on a single γ-Al_2O_3 pellet.[132] Analogous experiments were carried out with palladium ($PdCl_4^{2-}$) and it was found that adsorption of $PdCl_4^{2-}$ on γ-Al_2O_3 also causes an increase in the relaxation times of the fluids filling the pore system.[133]

The opposite influence of diamagnetic and paramagnetic adsorbates on the relaxation times of fluids in pores was used for studying the redistribution dynamics of $PtCl_6^{2-}$ and Cu^{2+} upon their simultaneous adsorption on the same alumina pellet. The results obtained showed that copper is gradually displaced inward from the surface of the pellet.[133, 134]

3. Rocks

Magnetic resonance imaging of brine-saturated sandstone rock cores and mapping the spin density and relaxation times of the spin systems in them has been reported.[86, 112, 135] The experiments revealed the presence of shale interlayers with small pore sizes and high content of clay, which appreciably suppress the amplitude of the water signal. Bedding planes $\sim$1 mm thick were also clearly seen in the images.[135] Analogous magnetic resonance images of limestone rock samples exhibited large voids and porosity variations. The signal amplitude and relaxation times distribution histograms of partially dried samples showed a much more inhomogeneous structure of limestone rock compared to the alumina structure.[86] Three-dimensional images of water or brine in rock cores revealed inhomogeneity of the porous structure or inhomogeneous saturation of the samples with water.[136] The results of the MRI studies of brine-saturated sandstone rock cores were compared with the data obtained by X-ray computerised tomography.[103]

The difference in the chemical shifts of water and dodecane was used for separation of their images in a sample comprised of two sandstone rock plugs placed one on top of the other, one of them being saturated with water and the other with n-dodecane,[95] and in a core saturated with a mixture of these fluids.[96] Two-dimensional chemical shift selective imaging of water and hydrocarbon in limestone rocks has also been reported.[94] In this case, a specified amount of hydrocarbon (water) was injected into the sample saturated with water (hydrocarbon). No complete displacement of one fluid by the other occurred. Experiments on displacement of H_2O by heavy water revealed the presence of a clearly seen interface between the two fluids. Two-dimensional images of kerosene distribution in a kerosene-saturated core are shown in Fig. 7.

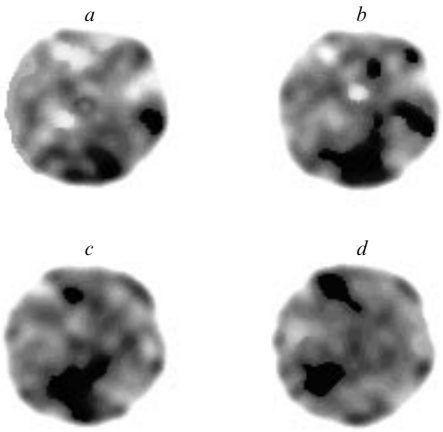


Figure 7. Sequential two-dimensional MRI images of adjacent slices of a kerosene-containing core. Darker regions in the image correspond to more intense NMR signal.
Each slice was 1.2 mm thick and the in-plane spatial resolution was 0.16×0.16 mm^2.

Separate three-dimensional images of water and motor oil in sandstone rock samples have been obtained on the basis of the differences in relaxation times.[100] Biexponential analysis of the relaxation decay curves obtained for each image pixel was used in studies of a chalk core saturated with water and petroleum crude.[101] The T_1 histograms exhibited two well-resolved peaks of finite width corresponding to the spin-lattice relaxation of water and petroleum. This allowed one to perform separate two-dimensional image reconstruction of water and petroleum, to establish that the regions with high concentration of water correspond to low content of petroleum (and *vice versa*) and to find cracks filled with water inside the core. Chemical shift selective imaging experiments were also carried out. The relaxation time histogram of the sample saturated only with water had one peak shifted towards longer times T_1 compared to the water peak of the preceding sample. This was explained by higher pore filing with water (assuming the same surface area of water contacting the pore surface) as a result of the removal of petroleum.

Magnetic resonance imaging studies of the dolomite cores dried under mild conditions and then saturated with oil[92] revealed the presence of cracks, voids and microporous domains. Experiments carried out taking into account the differences in the chemical shifts and relaxation times of water and oil revealed large amounts of residual water in the sample. The results were compared with those obtained by X-ray computerised tomography.

Multinuclear NMR has been investigated as a method for discriminating the contributions of the organic and aqueous phases to the NMR signal in studies of flooded petroleum crude cores.[104] To this end, a sandstone rock plug with four openings 0.5 to 2.9 mm in diameter was sequentially saturated with aqueous LiCl solution and pure trifluorotoluene and the three-dimensional images were recorded using the ^{7}Li and ^{19}F NMR signals.

The Earth is the largest sample that can be studied by NMR imaging technique. Simultaneously, this is the least effective magnet that is used in the NMR studies. To carry out the NMR imaging experiments in the geomagnetic field,[61, 137, 138] a 'hydroscope' device was created, which has been used in search for and the determination of the depths of occurrence and evaluation of the field volumes of proton-containing fluids at depths up to 200 m. A wire loop $\sim$100 m in diameter placed on the terrestrial surface is used for generation of the RF pulses and reception of the NMR signal. Very low signal-to-noise ratio is compensated by multiple accumulation of the NMR signal.

4. Polymers and gels

From the NMR standpoint, the properties of polymeric materials are intermediate between those of liquids and solids. This feature determines the choice of experimental techniques that can be used for studying this specific class of substances. Swelling of polymers in solvents allows imaging using the NMR signal of the solvent. Swelling also enhances the mobility of the polymer macromolecules, which sometimes permits a number of conventional liquid-state NMR techniques to be implemented to obtain the images of the polymer itself.[139, 140] In addition, an increase in size due to swelling allows better visualisation of the sample morphology.

The NMR images of a sample of a water-saturated polymeric composite reinforced with carbon fibre exhibited well-resolved structural defects filled with water.[141] These results were confirmed by sectioning the sample. If the size of structural defects and microcracks is smaller than the spatial resolution of the image, the amplitude of the NMR signal of the image pixel can be used for evaluating the defect size. Clearly, imaging of voids using the NMR signal of water is impossible; this can be done based on the NMR signal of the polymer itself.

Spin relaxation time measurements of polymers and gels allow one to obtain particularly valuable information. The time T_1 is sensitive to fast motions of atomic groups in the megahertz frequency range, while the times T_2 and $T_{1\rho}$ characterise slow, cooperative low-frequency motions and depend on the cross-link density and chain entanglement.[139, 140, 142] Useful information can also be extracted from the relaxation times of solvents since the behavior of the solvent molecules is to a great extent determined by their interactions with the polymer molecules.

Magnetic resonance imaging studies of swollen butadiene rubber [140] and *cis*-1,4-polyisoprene [142] of different initial compositions and cross-link density were carried out by detecting the NMR signal of the solvent (cyclohexane) or polymer (when cyclohexane-d_{12} was used).[139, 140] The images obtained exhibited clearly seen spatial inhomogeneities of the samples as well as structural defects and voids and allowed one to establish structural changes as function of the rubber vulcanisation time. Lower solvent concentration corresponded to the regions with higher cross-link density. The regions near the surface contacting the mould were characterised by higher cross-link density and by a decrease in the cross-link density as a result of reversion effects (at long vulcanisation times).[140] The signal intensity histograms constructed using the images obtained by solvent imaging technique can be used for characterisation of the cross-link density and sample homogeneity. The results of the T_2 measurements allowed one to assess changes in the molecular mobility. Analysis of the T_2 maps of the solvent showed [139] that the T_2 value is determined by the polymer – solvent interactions and the cross-link density. As the cross-link density increases during vulcanisation, the molecular motions slow down and the relaxation time T_2 of the polymer is shortened, thus weakening the NMR signal of the polymer. This revealed spatial inhomogeneity of the cross-link density distribution over the sample. The T_2 maps were converted into corresponding histograms. Analysis of the histograms showed that the T_2 distributions become narrower and their maxima shift towards shorter T_2 values as the vulcanisation time increases. There are in fact two T_2 values corresponding to the monomer units of the polymer chain located at long and short distances to the cross-link points.[139, 142] If triallyl cyanurate is used as vulcanising agent (at the vulcanisation temperature, this is a liquid whose mobility is sufficiently high for the domain formation), the polymers obtained are less homogeneous compared to those containing zinc diacrylate.

External perturbations can cause specific changes in the state of polymers and gels, *e.g.*, a temperature-induced volume-phase-transition. For instance, poly(*N*-isopropylacrylamide) gel swollen in water is in the equilibrium state at temperatures below the lower critical solution temperature (31 – 32 °C) and in the collapsed state above this temperature, the phase transition being reversible. The NMR images of this gel in different states, obtained using the

relaxation and diffusion contrast techniques provided an insight into the changes in the state of water and the mobility of the polymer molecules.[143]

Two-dimensional spin density and T_2 maps of water in a cross-linked poly(methacrylic acid) hydrogel were obtained.[144] Analysis of these maps revealed a uniform distribution and high mobility of the water molecules in the gel.[144] Applying mechanical stress causes a decrease in the content of water within the compressed region of the gel due to migration of water molecules to the surrounding uncompressed regions. The molecular motion of water in the compressed region of the gel becomes lower, which leads to shortening of the time T_2. Therefore, NMR imaging allows one to obtain information on the propagation of the strain induced by mechanical stress within the sample. Hydropolyelectrolyte gels can shrink in response to electric field. Imposing a voltage of 3 V across two platinum electrodes placed in contact with a gel led to its shrinkage which was larger near the positive electrode.[145] Using the two-dimensional gel images and T_2 maps, one can trace the changes in the shape of an initially cylindrical sample and determine the content and mobility of water in different regions of the gel sample. Analogous experiments were performed with the sample prepared using aqueous $MnSO_4$ solution and consisting of two parts with a different degree of cross-linking of the polymer.[146] The T_2 maps of water were converted into the Mn^{2+} ion concentration maps which showed that manganese ions migrate towards the negative electrode and this is responsible for the appearance of Mn^{2+} ion concentration gradients.

Nuclear magnetic resonance imaging has been used for quantitative studies of the properties of polysaccharide solutions and gels.[147] Gels were prepared by dialysing sodium alginate solutions against a solution containing calcium ions. The NMR images of the samples showed that the gels were inhomogeneous, that is, the gel concentration increased towards the centre of the sample. More homogeneous samples were obtained when NaCl was present in both solutions. The effect of the gel concentration (1% – 4%) and degree of O-acetylation on the relaxation times, diffusion coefficient and magnetisation transfer parameters was studied taking into account the exchange of water molecules between bulk water and the chemisorbed water.

Freshly prepared agarose gels are characterised by a single-exponential transverse relaxation and direct proportionality of the relaxation rate to the agarose concentration. This is associated with small sizes of structural inhomogeneities of the gel (< 0.3 μm). However, relaxation measurements performed after the 'slow freeze – thaw' cycle revealed a multiexponential behaviour. Crystal growth under conditions of slow freezing causes essential changes in the gel morphology, namely, the formation of structural inhomogeneities with a characteristic size of several micrometres, which are retained after thaw. Multiexponential behaviour of the transverse relaxation is due to the fact that diffusion of water cannot induce averaging at this length scale. On the other hand, the longitudinal relaxation is single-exponential for all samples. The results of experiments are in agreement with the data of calculations carried out based on a model which includes the relaxation due to proton exchange with hydroxyl groups and the physical interaction between water molecules and agarose spiral aggregates.[148] The T_1, T_2 and T_2^* maps of an Mn(II)-doped agarose gel and polyethylene have also been obtained.[149]

5. Suspensions, emulsions and compacts

Magnetic resonance imaging can be useful in nondestructive studies of fabrication of ceramics, *e.g.*, slip casting. For instance, cross-sectional two-dimensional images of a plaster of Paris mould filled with an aqueous Al_2O_3 suspension (initial content of water was 30 mass %) were obtained.[150] The images exhibited clearly showed suspension, and solid deposits on the mould walls and the mould walls themselves, through which water was removed. The suspension and the solid deposits were characterised by the same content of water; however, the relaxation times of water in these regions were appreciably different. Growth of the deposit layer with time was observed.

Ceramics can also be fabricated by pressure moulding. In this case, it is possible to study the distribution of organic components (binder, plastifier, anti-adhesives) within the sample, which has a strong effect on quality of the ceramic materials. Visualisation of the distribution of the polymeric binder in green ceramics allows sorting out substandard articles before reaching the dewaxing and sintering stages. Different strategies of magnetic resonance imaging and recording spatially resolved NMR spectra of a polymeric binder were compared taking the compacts prepared by compacting alumina powder mixed with polymeric binder (2.5 mass % or 15 mass %) as examples.[108, 151] No effect of the average particle size on the binder distribution was found; however, a decrease in the length-to-diameter ratio of the compact down to 0.17 led to increased concentration of the polymer around the periphery of the sample, which was associated with features of the pressing mechanics. The signal intensity histograms constructed based on the two-dimensional images of the compacts can be used for controlling the binder distribution homogeneity.[108] An NMR imaging study of a Si_3N_4 sample pressed in the form of a disk with openings of different diameters containing organic binder (15 mass %) has been reported.[151] The relaxation times of low-molecular-mass poly(ethylene oxide), polyvinyl alcohol and poly(ethylene terephthalate) used as binders in fabrication of ceramics are ~ 1 ms (T_2) and ~ 300 μs (T_2^*).[108]

When growing large zeolite crystals, it is important to know the mixing degree of the starting components. Nuclear magnetic resonance was used for the determination of the mixing quality of two starting solutions in a batch mixer.[152] The process was investigated under laboratory conditions. Zeolite A was synthesised from a sodium aluminate solution with triethanolamine (TEA) additives (TEA is an inhibitor of nucleation) and a silica suspension or sodium silicate solution. The NMR signal of the TEA protons was recorded; all other reagents were used in deuterated form. Analysis of the magnetic resonance images revealed the appearance of a large gradient of the TEA concentration after the first mixing cycle in the reaction with silica suspension. The concentration of TEA increased in a downward direction because of the higher density of the TEA – sodium aluminate mixture compared to the silica suspension density. Further mixing led to homogenisation of the TEA distribution in the mixture and after eleven cycles the mixture was almost homogeneous. The NMR images of the samples of the mixture exhibited clearly seen air bubbles trapped by the viscous medium. When the reaction was carried out with sodium silicate as the second component, homogenisation of the reaction mixture was even more complicated due to an increase in the viscosity of the mixture caused by gelation that started several seconds after placing the components in contact. Further mixing§ led to the formation of aluminosilicate hydrogel clots. Clots of different compositions are clearly seen in the magnetic resonance images. Analogous studies were also carried out during the synthesis of zeolite X. Attempts at using this approach to study the synthesis of mordenite failed. In this case, tetraethylammonium bromide (cross-linking agent) was used instead of TEA. Unlike TEA, this compound is not involved in complexation with aluminium or silicon and, hence, one cannot use its distribution for evaluating the mixing degree of the reagents.

The size and distribution of voids and gas bubbles in secondary explosives have strong effect on the initiation and propaga-

§ The efficiency of mixing strongly depends on the batch mixer design. The best batch mixer design was chosen based on analysis of the images of the samples obtained using four different types of batch mixers that were specially developed for the on-board synthesis of zeolites during space shuttle missions.

tion of detonation wave. The shock wave causes an adiabatic 'collapse' of voids, thus initiating a burst-like combustion. Void-containing samples can be obtained by mixing the explosives with hollow particles or by conducting a chemical reaction involving ammonium nitrate and sodium nitrite followed by liberation of dinitrogen. Concentrated oil-in-water emulsions can serve as examples of the secondary explosives. Two samples of the oil-in-water emulsions have been investigated.[153] One sample contained almost no voids while the other one was prepared using aqueous sodium nitrite solution to favour the formation of dinitrogen bubbles. Two-dimensional magnetic resonance images of the second sample exhibited voids of size up to 0.5 mm, whereas no voids were observed in the images of the first sample. These results are in agreement with the data of scanning electron microscopy studies.

Phase separation in the emulsion of sunflower oil in D_2O has been studied [154] taking a number of bulk samples and a sample prepared in the form of a film less than 600 μm thick as examples. Experiments revealed gravimetric separation of the dispersed phase from the continuous emulsion phase with time (creaming). An oil concentration gradient in the near-surface layer and an increase in the oil concentration with time were observed for all samples. Both facts seem to be associated with polydispersity of the sizes of the oil drops that become more 'close-packed' as a result of the action of the underlying layers.

6. Food products and plants

The potentialities of the MRI method in revealing the internal structure of and water distribution in the food systems containing small amounts of liquids was demonstrated [155] taking studies of the morphology of cookies, soft caramel with chocolate cream filler and a mixture of corn starch and water as examples.

Two-dimensional images and maps of the water spin density and T_2 distribution in plant tissues (Fig. 8) have been reported.[109] The relaxation time distribution maps give an accurate account of the peculiarities of the sample morphologies. For apples, the width of the NMR signal in a 4.7 T field is twice as large as that determined in the 2.35 T field. This is indicative of the local magnetic field gradients due to the difference in magnetic susceptibilities between the tissues and microscopic air bubbles.[156] Two-dimensional mapping of the distribution of the diffusion coefficient ($1.08-1.66\times10^{-5}$ cm^2 s^{-1}) and the RMS local magnetic field gradient (8.6–17.9 G cm^{-1} in the 2.35 T field) was also performed. Mealiness in apples and peaches stored under various conditions was assessed using MRI techniques.[157] Spatially resolved T_2 distribution maps were converted into corresponding T_2 histograms. Development of mealiness in apples leads to more pronounced asymmetry of the T_2 histograms. Analogous process in peaches causes transition from a Gaussian to a broad distribution with a flat top. This points to different physiological processes. The results of the MRI experiments were compared with the data obtained by conventional (mechanical) methods of fruit quality determination.

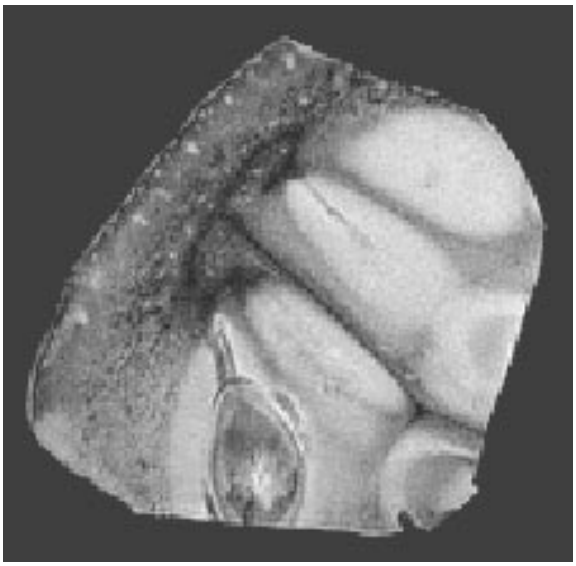


Figure 8. Two-dimensional MRI image of a fragment of a cucumber.

A MRI study of voidage in watermelons [158] involved recording the profiles of corresponding 1D projections on two orthogonal directions in the plane of a slice 20 mm thick. Then, these profiles were compared with analogous profiles expected for an ideal sphere. Out of 30 samples, 28 watermelons were correctly identified, which was confirmed by two-dimensional imaging.

Heat stress can retard the ripening of many fruits. Studies of tomato fruits kept at 42 °C revealed no changes in the size and overall content of water.[159] After 36 h the relaxation times T_1 and T_2 of water remained unchanged in the pericarp and became shorter for all other plant tissues. Then, the fruits were kept at 25 °C for 24 h; however, no lengthening of the relaxation time T_2 up to the initial value was observed. Probably, heat stress causes the formation of associates of some unbound water molecules with denatured proteins. No complete regeneration of the structure occurred during 24 h after heat stress, which seems to be responsible for a 120 h delay of change in colour, though the rate of ethylene and carbon dioxide production recovered virtually immediately after return to ambient temperature.

Bulk analysis of tobacco and cigarettes by magnetic resonance imaging was performed to map the spin density and relaxation time distributions.[160] The more mobile components (water and tobacco wax) were spin echo imaged while the solid components (cell wall polymers) were observed using the SPI technique. More dense packing of tobacco and lower content of water at the cigarette tip was pointed out. The region near the lateral surface of the cigarette is characterised by higher content of water in tobacco. Partial redistribution of water from tobacco to the filter region was also observed.

Knowledge of the internal morphology of wood is of great importance for wood-working industry. For instance, the possibility of revealing internal (hidden) defects of a log allows one to determine an optimum strategy of sawing beforehand. Cross-sectional two-dimensional images of white oak and black cherry samples 15 to 25 cm in diameter exhibited clearly seen heart-wood and sap-wood regions, the pith, the medullary rays and the growth rings.[161] Besides, the eccentricity of the growth rings in the image pointed to the presence of the tension wood which is indistinguishable by the naked eye. The wet-wood region, which is hard to dry, looks as a bright strip in the image. Some water is evaporated through the cracks in the bark during long-term bulk storage of wood. As a result, the sap-wood contains regions characterised by the NMR signals of low intensity. For black cherry, the pith and the medullary rays are indistinguishable in the image owing to their small size; however, one can see gum spots, which are hard to polish when working, as well as hidden knots and scars, wormholes and wood decay regions. The bark cannot be seen in the images because of the low content of water. Magnetic resonance imaging studies of plant roots have also been reported.[162, 163]

7. Other materials

Three-dimensional images of the distribution of mobile components in coal were obtained in the temperature range from 25 to 475 °C.[164] It was found that this distribution is inhomogeneous and different for different sorts of coal. The fraction and homogeneity of distribution of the mobile proton-containing component increase as the temperature increases up to 450 °C and then dramatically decrease at higher temperatures as a result of sintering and coking.

Ice coated with gas hydrate melts at room temperature. The process involves the formation of liquid water encapsulated into a solid shell and the sample looks as a white powder-like solid. The

gas hydrate coating is formed in the reaction of ice crystals with CD_4 or xenon at high pressure.[165,166] Hyperpolarised xenon [167–170] was used in studies of the formation of clathrate hydrates and in measurements of the rate constant for this process. Confirmation of the fact that the activation energy is negative [171] was also obtained in the experiments with hyperpolarised Xe.

The distribution of water in foam churned from egg white and water has been studied.[172] As time passes, the content of water increases in the lower part and decreases in the upper part of the sample (the liquid flows down under the action of the gravity force). This is accompanied by an increase in the relaxation time T_2, which can be associated with growth of the foam bubbles. For the foam prepared by shaking water with additives (surfactants, polymer and alcohols), the upper part of the sample was characterised by a reduced spin density; this visually corresponded to much larger bubbles compared to those in the other regions of the sample.[173] Transformation of essentially non-rectangular water distribution profiles with time was compared with the results of model calculations carried out with inclusion of the downward flow of the liquid under the action of the gravity force. It was found that the model incorrectly describes the early stages of the process; however, it provides an adequate description at long times.

The 1D MRI profiles were also obtained, which illustrated the phase separation in the critical binary mixture aniline–cyclohexane after cooling below the upper critical equilibrium temperature.[121]

IV. NMR porosimetry

1. General remarks

In this Section we will consider some methods of the pore size determination based on the effect of the pore sizes on the nuclear spin relaxation times or on the freezing points of liquids in porous media. Besides, many other NMR measurements are to some extent sensitive to the pore size and other characteristics of the pore space. If pores are larger than 10 μm, their exact sizes can be determined by direct visualisation of the liquid that fills the pore space. Information on the pore sizes and tortuosity of the pore space can be extracted from, *e.g.*, the results of measurements of the diffusion coefficients of fluids that fill the pores.[25,174–179] The chemical shifts of the substances adsorbed from solution on the surface [180] and of the adsorbed gases (first of all, xenon [181–185]) are sensitive to the pore size. The pore size distribution determines the shape of the water distribution profiles recorded during drying of liquid-saturated porous materials.[186–188] The local magnetic field gradients can also reflect the shape and sizes of pores.[189,190]

The properties of the molecules of a liquid contacting a solid can be substantially different from the properties of bulk liquid. For instance, the properties of water adsorbed on the surface of silica glass are strongly different from those of bulk water due to the formation of hydrogen bonds with the surface hydroxyl groups.[191] This leads to, *e.g.*, reduction of the density of the surface water layer, considerable reduction of rotational mobility of the molecules, anisotropy of the molecular mobility and to the freezing point depression. The NMR properties of the molecules that interact with the surface also change.

Most of the experiments on the NMR porosimetry were carried out without spatial resolution; however, this method can also be used in combination with the MRI technique. In the latter case, it is possible to determine the average pore size (or even the pore size distribution) and the pore volume (this parameter correlates with the local porosity of the sample) for each image pixel.[110] It should be mentioned that the changes in the T_1 and T_2 values caused by the interaction with the surface can lead to relative enhancement or suppression of the NMR signal near the macroscopic interfaces when using relaxation-weighted imaging and that the liquid in the smallest pores can have very short relaxation times T_2 and make no contribution to the NMR signal.

2. Relaxation porosimetry

Often, the spin relaxation (T_1, T_2, T_2^*, $T_{1\rho}$) in a liquid or gas contacting the surface of a solid occurs much faster than in the bulk. Detailed NMR investigations of the surface relaxation have been carried out for long. The results of the early studies of the relaxation of the liquids contacting solid silica (silica gel), alumina, coal and zeolite surfaces were generalised by Packer.[192]

One of the reasons for higher relaxation rate of the nuclear spins of the fluid molecules contacting the surface is a substantial change in the correlation time of molecular motions caused by changes in the mobility of the molecules located on the wall or in the near-wall region. Besides, either the interaction between protons of the liquid and the spins of hydrogen atoms of the surface hydroxyl groups or proton exchange can produce additional fluctuating magnetic fields.[148,193] Paramagnetic ions or other paramagnetic centres that can exist on the surface or in the near-surface layer of the solid have the strongest effect on the relaxation of fluids.

The relaxation of liquids in silica-based rocks (sandstone rocks) is mostly associated with the presence of paramagnetic ions (*e.g.*, iron or manganese ions).[194,195] Their concentration can be as high as several per cent, the iron ions being more abundant.[196] In this case, relaxation is due to the dipole and scalar interactions between the electron and nuclear spins. These interactions are frequency modulated by the relaxation flips of the electron spin and by finite residence time of the molecule on the surface of the solid. The latter reason seems to be insignificant since no pronounced temperature effect was observed.[194] In addition, sandstone rocks sometimes contain particles of magnetic minerals, such as magnetite (Fe_3O_4), which favour an increase in the relaxation rate.[197] Often, sandstone rocks contain clays that possess a rather large specific surface area but have weaker effect on the relaxation parameters.[196] Carbonates are characterised by longer relaxation times compared to sandstone rocks.[197]

The relaxation times of systems containing several liquids can strongly depend on the wettability of the pore surface and on the procedure for sample preparation (*e.g.*, on the order in which the pores are filled with different liquids). For instance, experiments with hydrocarbons and water contained in the pores of rock samples showed that the former have longer relaxation times than the latter. This is presumably due to the presence of a monolayer of water on the pore surfaces even in the initially dried samples.[194]

Exchange between the surface layer and the bulk of the liquid or gas in the pore is responsible for a finite residence time of the molecules on the surface. The exchange rate strongly affects the results of measurements. The evolution of the magnetisation of a liquid in an isolated pore was studied in detail earlier.[198,199] In the case of slow exchange the amplitude of the relaxing magnetisation is different at different distances from the pore surface and the relaxation behaviour is a multiexponential superposition of the amplitudes of the magnetisation of different pore regions. At moderate exchange rates, interpretation of the relaxation behaviour is complicated. For a binary system with two times T_1, the magnetisation relaxation is described by a sum of two exponents; however, the T_1 values and the contributions of the two components can be substantially different from true values. Moreover, at $T_1 > T_2$ the T_2-relaxation can exhibit a biexponential behaviour while the T_1-relaxation can remain single-exponential.[192] The times T_1 and T_2 of the molecules in the surface layer can mainly be determined by different motions (*e.g.*, molecular rotation and reorientation of the axis of rotation).

The simplest case is fast molecular exchange between the near-wall layer and the volume of the pore (fast diffusion or slow surface relaxation). In this case the liquid in the pore exhibits a single-exponential relaxation behaviour even provided a non-

exponential temporal dependence of the relaxation of the molecule located on the pore wall. This holds if [200]

$$T_1 > \frac{r^2}{6D}, \tag{8}$$

where r is the pore radius and D is the diffusion coefficient of the molecules of the liquid. This condition is met if $r < 10-100$ μm (*e.g.*, for many sandstone rocks). In this case, the simplest model of relaxation of the liquid in the pore is a two-site model with fast exchange, according to which [201]

$$\frac{1}{T_1} = \frac{a}{T_{1v}} + \frac{b}{T_{1p}}, \tag{9}$$

where a and b are the fractions of the liquid in the bulk and on the surface, respectively; and T_{1v} and T_{1p} are the corresponding relaxation times T_1. The volume of the surface layer is often assumed to be equal to the product of the pore surface area, S, and the layer thickness, λ, though this can be not universally true for the smallest pores owing to high curvature of their surfaces.[202] Then one gets [194]

$$\frac{1}{T_1} = \left(1 - \frac{\lambda S}{V}\right)\frac{1}{T_{1v}} + \frac{\lambda S}{V}\frac{1}{T_{1p}} \approx \frac{1}{T_{1v}} + \rho_1 \frac{S}{V}, \tag{10}$$

where V is the pore volume and ρ_1 is the surface relaxivity of the nuclear spins.

The reasons responsible for shortening of the times T_1 also cause shortening of the times T_2 of the liquid in pores. In addition, the rate of the transverse relaxation also increases due to molecular diffusion in the presence of local field gradients that can be produced owing to inhomogeneity of the external magnetic field near the boundary between the phases with different magnetic susceptibilities.[86, 203] Therefore, the T_2 time distribution allows characterisation of the pore sizes only if the experiments are carried out in relatively weak fields (< 500 G) and/or with multiple refocussing of the NMR signal using the CPMG pulse sequence. In this case, one can write for T_2 an expression analogous to Eqn (10):

$$\frac{1}{T_2} = \frac{1}{T_{2v}} + \rho_2 \frac{S}{V}. \tag{11}$$

Often, the first term in the right side of expressions (10) and (11) is small and can be neglected.[194]

Interpreting the T_2 values is a challenge;[204] nevertheless, relaxation porosimetry based on the T_2 measurements has found a number of practical applications. To take into account the effect of the local magnetic field gradients on the T_2 values, the parameter ρ_2 is sometimes assumed to be a function of the applied magnetic field. This implies a non-spherical shape of the pore; otherwise, application of external magnetic field cannot produce local field gradients. However, the pore surface is not ideally smooth; therefore, even for a spherical pore one should expect rather large local field gradients in the immediate vicinity of the surface.[205]

If all pores have an identical shape, the V/S ratio is a measure of the pore size. In the case of non-spherical pores (long cylindrical pores or slit-like pores) the relaxation porosimetry measurements are sensitive to the smaller size.[204] Determination of the pore size requires knowledge of the surface relaxivity which can be found from calibrations which utilise sample-independent techniques of pore size measurements. In practice, the surface of the pore space has fractal character (that is, the measured value of the surface area is a function of the length scale that is used for measurements). Therefore, the surface relaxivity values strongly depend on the type of the sample-independent calibration technique. In particular, the V/S ratio and the surface relaxation parameters can be extracted from an analysis of the results of the effective diffusion coefficient measurements of the gas or liquid molecules in the pores, as it was done in, *e.g.*, studies of some natural rocks.[174] Another procedure for determining the ρ_1 and ρ_2 values involves measurements of the relaxation times using the samples characterised by a monolayer coverage of the surface of the pore space.[206] For the model media (*e.g.*, bead packs), the V/S ratio can be calculated.[207]

The surface relaxivity values vary over a wide range from 10^{-7} to 10^{-3} m s^{-1}. For water in synthetic materials the ρ_1 values usually span the range from 1×10^{-4} to 20×10^{-4} m s^{-1} (see Ref. 196). Typical of water in sandstone rocks are the values $\rho_1 \sim 2.5\times10^{-6}$ m s^{-1} and $\rho_2 \sim 5\times10^{-6}$ m s^{-1}, while water in carbonate rocks is characterised by the parameters $\rho_1 \sim 0.8\times10^{-6}$ m s^{-1} and $\rho_2 \sim 1.7\times10^{-6}$ m s^{-1}. Experiments with different samples of natural rocks showed that the ρ_1 value varies only slightly despite the fact that the concentration and type of paramagnetic impurities can vary over a wide range from one sample to another (see below). The ρ_1 parameter of water in limestone rock, chalk and sandstone rock cores was reported to vary from $\sim7\times10^{-6}$ to 23×10^{-6} m s^{-1}.[207]

The effect of paramagnetic ions on the relaxation times of liquids has been studied in detail. For instance, calcite powder packs with known concentration of manganese were prepared by centrifuging the suspension of calcite particles (10 or 30 μm) in water with addition of aqueous $MnCl_2$ solution.[195] Then, the surface layer of the liquid was removed. For all samples, the spin-lattice relaxation was found to be single-exponential. The specific surface areas of the powder packs were measured using low-temperature adsorption of nitrogen. It was found that high concentrations of adsorbed manganese increased the parameter ρ_1 by a factor of ~50 (up to a value of 2.4×10^{-5} m s^{-1}) and that an increase in the initial concentration of manganese led to saturation of this parameter. This can be the reason why various natural rock samples are characterised by similar ρ_1 values. Moreover, long contact times of calcite with manganese caused a decrease in the ρ_1 value despite an increase in the amount of the adsorbed manganese. Presumably, some adsorbed manganese becomes buried by freshly precipitated calcite. NMR experiments revealed that only the ions in the outermost atomic layer affect the relaxation. Analogous experiments with Co^{2+} ions showed that these ions have virtually no effect on the relaxation times of water, whereas adsorbed iron ions shorten the T_1 value of water (however, to much lesser extent compared to Mn^{2+} ions). Thus, relaxation owing to the presence of manganese predominates for limestone rocks and possibly plays an important role for sandstone rocks. Flowing a 4 μM aqueous solution of a Mn^{2+} salt through a sample of natural limestone rock led to a decrease in the T_1 value of water by a factor of ~6 due to adsorption of Mn^{2+} ions on the surface. Partial desorption of manganese and dissolution of the sample under the action of an aqueous solution of ethylenediaminetetraacetic acid caused partial recovery of the initial T_1 value of water.

Kleinberg *et al.*[196] prepared powder packs of the α-modification of calcium silicate with known concentrations of iron or manganese paramagnetic ions by centrifuging suspensions in water and measured the relaxation times T_1 and T_2 of the samples with different content of Mn and Fe. It was found that the T_1 and T_2 values are virtually temperature independent in the range between 25 and 175 °C. Hence, diffusion, molecular motions and the residence time play an insignificant role and the surface relaxation cannot be due to thermally activated processes such as adsorption and translational and rotational motions. The parameters ρ_1 and ρ_2 were found to be linearly proportional to the manganese and iron concentration, the slopes of the corresponding plots constructed for Fe and Mn being comparable in magnitude. In the limit of zero concentration of these elements, the ρ_1 and ρ_2 values can be determined by the concentration of point defects on the crystal surfaces. Clay-bound water does not mix with water filling the pores and gives a separate peak in the T_2 distribution.

Clearly, in real porous media the pores are interconnected and voids are not filled with fluid. Therefore, the model of the evolution of the magnetisation in isolated pores[198, 199] is a particular case of a more general model that treats a system of pores filled with a fluid and interconnected by narrow channels.[208] If no fluid transport occurs in the system of pores, the relaxation time distribution corresponds to a superposition of the relaxation times of the fluid in individual pores. If the connectivity of the system of pores is low, the relaxation time distribution is broadened and shifted towards shorter times. If the connectivity of the system of pores is high, the relaxation time distribution again becomes narrower and exhibits a maximum at a value determined by the ratio of the total surface area to the total volume of the pores in the sample. If the pores are connected by very narrow channels, the latter can act as efficient relaxation sinks. From the standpoint of the fluid relaxation measurements, this allows one to treat the pores as isolated.[201, 209] It should be emphasised that if the surface relaxation dominates, the rate of the change in the magnetisation at short times is proportional to the ratio of the total surface area to the total volume of the pore space irrespective of the pore system connectivity.

Samples of synthetic porous materials are characterised by relatively small structural inhomogeneities. Therefore, the molecules have time to 'explore' the pores of all sizes during the NMR experiment; this often leads to single-exponential relaxation. On the other hand, relaxation of fluids in rocks is non-exponential since the observation time is too short for the molecules to travel the distances comparable with the length scales of structural inhomogeneities.

Thus, if pores can be considered isolated in the time scale of the NMR experiments, the magnetisation relaxation is a superposition of the contributions of pores of different sizes and the relaxation time distribution correlates with the pore size distribution. The results of relaxation measurements are analysed using the average T_1 value or a number of models that represent the experimental data by the sum of several (from 1 to 3) exponents or as stretched exponential functions

$$M_{xy}(t) = M_0 \exp\left[-\left(\frac{t}{T_2}\right)^{\alpha}\right], \tag{12a}$$

$$M_z(t) = M_0\left\{1 - 2\exp\left[-\left(\frac{t}{T_1}\right)^{\alpha}\right]\right\}. \tag{12b}$$

Computer simulation of the magnetisation relaxation by the random walk method showed that expressions of the type (12) are physically substantiated. However, this model has a significant drawback consisting in the impossibility of back extrapolating the experimental data to time zero at $\alpha < 1$, which precludes a correct estimation of the spin density (amount of fluid). To overcome this problem, a modified model [210] has been suggested

$$M_{xy}(t) = M_0 \exp\left[-\frac{t}{\tau_0}\left(1 + \frac{t}{\tau_c}\right)^{\beta-1}\right], \tag{13}$$

where τ_0, τ_c and β are empirical parameters.

At short times, this function describes a single-exponential decay corresponding to the weighted sum of the initial rates for each relaxation time in the entire distribution of relaxation times. At long times, the function is transformed into expression (12a). Using this model, relaxation measurements of a total of 50 rock samples saturated with different fluids were carried out in different magnetic fields. The model (13) exhibited some advantages in determining the amount of fluid by back extrapolation of the experimental data to time zero, especially for partially saturated samples after centrifuging. Correlation between the parameters of the model and the petrophysical properties of the samples has been discussed. Applicability of the model for representing the T_1-relaxation data has been pointed out.[210] The virtue of the models (12) and (13) is their compactness.

Theoretical approaches involving either discrete or continuous distributions, $f(T_1)$, have been widely used in fluid relaxation studies. In this case, the magnetisation relaxation is described by the following expression

$$M(t) = M_0\left[1 - 2\int_0^{\infty} f(T_1)\exp\left(-\frac{t}{T_1}\right)\mathrm{d}T_1\right]. \tag{14}$$

Using appropriate models, the $f(T_1)$ distributions can be converted into the pore size distributions. For rocks, the T_1 values usually span the range from 1.5 to 3 orders of magnitude. Reconstruction of the relaxation time distribution function from experimental data is an ill-posed problem. Solving this problem requires specific theoretical approaches (*e.g.*, regularisation).[203, 207]

Typical of many samples is fast diffusion within pores. This is confirmed by, *e.g.*, the lack of strong temperature dependence of the relaxation times in the range between 25 and 75 °C, which indicates that diffusive motion is not a rate-limiting process.[194] In this case, each pore of a particular size is characterised by exponential relaxation with its own time constant T_1. More sophisticated models involve a multisite exchange and a number of T_1 values for arbitrary rate of exchange between the components within each pore. This is significant for mesoscopic and macroscopic pores in which the fast diffusion limit cannot be reached. For instance, relaxation of the longitudinal magnetisation was simulated with a pore size distribution in the form of a sum of three log-normal distributions. The procedure was evaluated using a model data set with known pore size distribution and the factors affecting the reliability of the reconstructed pore size distribution were analysed.[201] The results of computer simulation of the experimental T_1 measurements allowed one to obtain the pore size distributions for brine-saturated sandstone rock and limestone rock samples.[209] The ρ_1 value was assumed to be 10^{-4} m s^{-1}. Inapplicability of this technique to large pores (hundreds of micrometres) due to the loss of sensitivity to the exact shape of the pore size distribution was pointed out.

In the case of (quasi-)continuous distributions the values of the function $f(T_1)$ are often reconstructed [211] using a discrete set of argument values ($\sim$100 points). This is an ill-posed problem complicated by noisiness of the experimental data. Considerable attention has been given to solving this problem.[212] The major drawbacks of most of algorithms consist in broadening sharp $f(T_1)$ peaks and replacing broad $f(T_1)$ distributions by a set of narrower peaks. An algorithm has been proposed, which is free from these drawbacks.[212, 213] The procedure was evaluated taking a model data set as an example and then used for reconstruction of the function $f(T_1)$ for a number of samples of water-containing ceramics and brine-saturated sandstone rock cores.

The nuclear spin relaxation times of water in crushed porous glass of different pore sizes and amounts of the adsorbed fluid were studied.[191, 214] Nearly single-exponential relaxation (T_1, $T_{1\rho}$, T_2) was observed in all the experiments. The measured relaxation times were analysed in the framework of the model of fast proton exchange between the surface layer and bulk water. The relaxation times of water in the first monolayer were found to be $T_1 = 150$ and $T_2 = 0.5$ ms.[214] Relaxation (at least, the T_1 relaxation) is due to modulation of the dipole–dipole interaction of the nuclear spins, which allowed one to estimate the correlation times, τ, of rotational molecular motion. It was found that $\tau \sim 20\tau_0$ for water in the first monolayer, $\tau \sim (6-10)\tau_0$ for water in the second monolayer and $\tau \sim \tau_0$ for the rest of adsorbed water, where τ_0 is the correlation time of bulk water (of the order of 10^{-11} s), the lifetime of the water molecules in each state being no longer than 0.5 ms.[214] According to the results of $T_{1\rho}$ dispersion measurements (dependence on the amplitude of the RF field in the spin-locking experiments), fast rotational motions with a characteristic correlation time of 10^{-8} s are accompanied by much slower motions, namely, reorientations of the rotation axis of the molecule after every 10^{-5} s.[191]

Correctness of the relaxation model was confirmed by the results of relaxation studies with controlled variation of pore saturation level which was achieved either by adsorption of a known amount of liquid by a dry sample or by centrifuging a saturated sample.[194, 204] In the latter case, an increase in the centrifugation rate led to removal of the liquid from progressively smaller pores. Experiments with water in porous glass showed that smaller pores have a stronger effect on the relaxation times [191] that are shortened as the pore saturation level decreases,[191, 214] which is consistent with the relaxation model.

Gradual increase in the content of water in silica samples with different pore sizes revealed the biexponential T_2 relaxation.[202] A model of the pore filling with water, which takes into account the dependence of the contributions and the individual relaxation times of the two water components, is as follows. Initially, an increase in the pore saturation level leads to an increase in the surface area covered by the water monolayer and to an increase in the number of the smallest water droplets at the pore corners. Then the surface is covered by the second monolayer of water molecules while water droplets begin to grow and merge until complete filling of the pores. Another picture was observed for cyclohexane in conventional silica and for water in hydrophobic silica with methyl groups attached to its surface. In these cases the pore filling occurred uniformly starting from the smallest pores. Analysis of the experimental data allowed determination of the surface-area-to-volume ratio for water and of the number of water droplets at the pore corners at different saturation levels.[202]

Various rock cores saturated with water or brine have been studied using controlled variation of the saturation level. Computer simulation of the relaxation data was carried out with the sum of three exponents,[200] expressions of the types (12a) and (12b) [206] or with continuous relaxation time and pore size distributions.[92, 207] In all cases, the measured relaxation times agreed with the assumption that during the saturation process the smallest unoccupied pores are filled out first, while during the drainage the largest occupied pores are first to be emptied. The pore size distribution peaks also shifted towards smaller pore sizes, which can be associated with the presence of partially filled pores.[207] It was found that the relaxation times of water in sandstone rock [206] are temperature independent in the range between 13 and 60 °C and that the T_1/T_2 ratio lies between 1.4 and 3.2. The longest-to-shortest T_1 ratio is 1800, which is in satisfactory agreement with the largest-to-smallest pore radius ratio in the sample.[200] Analysis of results of measurements at different saturations allowed extraction of the pore size range without determining the S/V ratio for the entire sample with completely filled pores. It was found that the relationship between the average relaxation time and the saturation level (C) has the form

$$\langle T_1 \rangle = 1.29\, C^{1.26}. \qquad (15)$$

This correlation can be useful when determining the absolute values of saturation levels of the sample from relaxation measurements.

Agreement between the calculated and experimental data can be substantially improved by using a model with inclusion of narrow inter-pore channels that are filled first, thus determining the relaxation properties at low saturations.[206] This allowed one to estimate the volume ($\sim$4.5%) and diameter (0.75 μm) of these channels. The channel size is in agreement with the observed water–vapour percolation threshold occurring when the thickness of the adsorbed layer becomes equal to the radius of the channel. The pore sizes obtained from mercury porosimetry studies are by an order of magnitude smaller since this technique is mostly sensitive to the sizes of the inter-pore throats.[207] Mass transport can alter the NMR signal from the liquid in small pores. The residual saturation is due to the presence of capillary-bound water and, probably, water in isolated cavities.[92]

Spatially resolved relaxation porosimetry experiments are also possible. This allows mapping the pore saturation level and pore sizes for each pixel of the image. For instance, catalyst granules [110] and water-saturated sandstone rock cores were studied using this technique. Some samples were modified by attaching a silane chain to the surface of the pore space.[90] The experimental porosity values of these samples were found to be in agreement with the results of mercury porosimetry measurements. It was found that modification of the surface causes a twofold increase in the T_1 and T_2 values of water in pores, which permits wettability studies of the surface of the pore space. The modified sample was characterised by equal T_1 values of the surface water and bulk water, which means that the surface has no effect on the spin-lattice relaxation.

Relaxation porosimetry can also be applied to studies of other materials. In particular, the sizes of the pores left in the food systems and gels after freeze-drying at a reduced pressure characterise the sizes of initial ice crystals. Knowledge of the size distribution allows optimisation of sublimation conditions to improve, *e.g.*, quality of food after thaw. For instance, starch gel was freeze-dried at a reduced pressure and then filled with acetone.[205] Samples of different compositions were studied at different freezing rates and the T_2 distributions were determined (T_2 values varied from 55 ms to 2.5 s). Measurements in different magnetic fields revealed rather large local field gradients. Freezing of a cylindrical sample caused the formation of ice crystals (pores), whose sizes increased in the radial direction from the centre to the surface of the sample. The pore sizes in the samples of 10% and 15% gels were different. Calculations performed assuming spherical pores led to the ρ_2 values spanning the range from 1.2×10^{-5} to 4.2×10^{-5} m s^{-1}, which is of the same order of magnitude with the surface relaxation coefficient at the water/glass interface (3.5×10^{-5} m s^{-1}). The results of these experiments were compared with those of the scanning electron microscopy studies.

Nuclear magnetic resonance logging is one of the most prominent examples of practical implementation of the NMR porosimetry. Borehole logging is used in studies of the deep-earth properties of rocks. One of the most important applications of this method is investigation of the properties of the petroleum and gas fields (in particular, determination of the content of petroleum, gas and water and studies of the interactions of these fluids with rocks). The NMR logging experiments involve lowering a device containing the source of the magnetic field (a magnet or a coil) and a RF coil for creation of the RF field and reception of the NMR signal down a borehole. In this case, the NMR signal comes from the region that is outside the device (within the thickness of the rock mass) [197, 215–218] at a depth up to several centimetres from the borehole wall. (For comparison, in an NMR spectrometer the sample is located inside the probe). There is a number of different designs of the NMR logging devices.[197] All of them use relatively low magnetic fields; therefore, only the ^{1}H NMR measurements provide sufficiently high sensitivity. Weak non-uniform magnetic field precludes separation of the contributions of the hydrocarbons and water to the NMR signal based on the chemical shifts.[197] On the other hand, the amplitude of the NMR signal characterises the content of the fluid while the relaxation times correlate with the pore sizes and the types of the fluids filling the pores. This allows determination of such borehole characteristics as the free fluid index, porosity and rock permeability.[219] Because of the low sensitivity of the method, the T_2 measurements are most often used since they can be performed much faster compared to the T_1 measurements. The relaxation times T_2 of unbound fluid are usually much longer than those of the bound fluid; therefore, analysis of the results of measurements of the T_2 distributions permits separation of the contributions of the unbound and capillary-bound fluid.[197, 219] Most of rocks possess hydrophilic properties; therefore, the hydrocarbon is at the centre of the pore and does not contact the surface. In this case, the relaxation times of the hydrocarbons of low viscosity are much longer than those of water, which makes it possible to separate their contributions to the NMR signal.[197] Using empirical correlations between the viscosity and the T_2 values of hydrocarbons, one can determine the properties of the hydrocarbon pools and the hydrocarbon

type.[219] Based on the knowledge of the pore size distribution, the permeability of and the capillary pressure in porous media can be estimated. It was empirically found that the permeability of water-saturated sandstone rocks is proportional to the square of the relaxation time.[197] This is in agreement with expressions (10) and (11) assuming the rock permeability to be proportional to the $(S/V)^{-2}$ ratio.

The contributions of water and hydrocarbons to the NMR signal can be separated even at equal relaxation times.[219] To avoid explosive outbursts, drilling is carried out under excessive pressure which causes permeation of the fluid from the borehole into the rock. Therefore, the near-wall region used for the NMR measurements contains a mixture of the formation and borehole fluids. By doping the fluid injected in the borehole with water-soluble paramagnetic additives one can substantially shorten the relaxation times of water in the rock without changing the relaxation rates of hydrocarbons. In practice, a number of different types of the logging devices is simultaneously lowered down the borehole. Comparison of the results obtained by different methods allows better characterisation of the borehole.

3. Cryoporosimetry

Using the NMR technique, one can easily distinguish between the fluid and the solid based on considerably different relaxation times. For instance, freezing of water leads to shortening of the time T_2 from 1.8 s to 6 μs (see Ref. 220). A short time T_2 means that the transverse magnetisation (the NMR signal) experiences a rapid decay. Therefore, the use of a time delay of the order of 20 μs before recording the free induction decay or the recording of the spin echo signal allows one to exclude the contribution of the frozen fluid to the NMR signal. In addition, the T_1 value of ice ($\sim$900 s at 263 K in a 7.05 T field)[221] much exceeds the T_1 value of liquid water (2.7 s). Hence, the NMR signal of ice is additionally suppressed due to saturation. This permits selective detection of the signal of the liquid phase (see Fig. 6).

The pore liquid has a lower temperature of the liquid–solid phase transition. This effect is analogous to the capillary effect and is a result of a change in the free energy caused by the curved surface of the liquid. Reduction of the temperature of the liquid–solid phase transition can be described by the Gibbs–Thomson (Kelvin) equation written in the form[222, 223]

$$\Delta T = T_0 - T_c = \frac{2\sigma T_0}{R\Delta H\rho} = \frac{K}{R}, \tag{16a}$$

or as follows[221]

$$\Delta T = T_0 - T_c = \frac{K}{R-d}, \tag{16b}$$

where T_0 is the phase transition temperature for the bulk liquid; T_c is the phase transition temperature for the pore liquid; σ is the surface energy at the liquid–solid interface; R is the radius of ice crystal; ΔH is the molar heat of fusion; ρ is the density of the solid; and d is the thickness of the surface layer which freezes at a lower temperature compared to the rest of the liquid in the pore of radius R. The parameters K and d depend on the nature of the system under study. The surface layer behaves as part of the pore surface;[224] therefore, the pore radius is $R-d$. Sometimes, calculations give negative values of the parameter d and this interpretation loses its meaning. After rewriting[225] expression (16b) in another form

$$\Delta T = T_0 - T_c = K^* \frac{R}{R-d}\frac{1}{R}. \tag{16c}$$

one gets a new physical interpretation, namely, the molar heat of fusion that appears in the expression for K becomes pore size dependent.

The parameter K can be found by comparing the results of the NMR experiments with the data obtained by conventional methods, *e.g.*, low-temperature adsorption of nitrogen. The parameters for water were found to be $K_w = 495$ K Å, $d_w = 3.5$ Å,[224] and $K_w \approx 515$ K Å and $d_w \approx 3$ Å.[225] Benzene ($T_0 = 278.5$ K) or cyclohexane ($T_0 = 279.5$ K), which are more sensitive to small variations of temperature, are used instead of water in the case of large pore sizes. The parameters for cyclohexane are $K_c \approx 1800$ K Å (see Refs 222 and 226) and $K_c \approx 870$ K Å, $d_c \approx -1.4$ Å[225] while those for benzene are $K_b \approx 1100$ K Å and $d_b \approx 7$ Å.[225] For all liquids, the parameter K was found to be only slightly dependent on the nature of the porous material.[224] Formulae (16b) and (16c) lose their meaning at $R \leqslant d$; in addition, the filling of micropores is strongly affected by the properties of the fluid and the microporous material. Therefore, the application of this method to microporous objects is still to be clarified. Nevertheless, the technique allows experimental determination of the volume fraction of micropores.[224]

Nuclear magnetic resonance porosimetry experiments with slow cooling of the pore fluid or heating of a preliminarily frozen sample are used to obtain the plots of the dependences of the integrated amplitude of the NMR signal on temperature (*IT*-curves) or on the inverse temperature $I(1000/T) = I(X)$. For some samples the cooling–heating cycles exhibit hysteresis effects of the order of several degrees. Often, measurements are carried out only during heating the sample to avoid supercooling of the fluid. The experimental data should be processed taking into account the temperature dependences of other parameters affecting the NMR signal, such as the Boltzmann factor (Curie law), the Q-factor of the RF coil and the relaxation times. Usually, the integrated intensity of the NMR signal is determined to an accuracy of several per cent.

Often, experiments are carried out with excess amount of fluid to ensure a complete pore filling. The fluid on the outer surface of the material freezes at the normal freezing temperature and is readily distinguishable in the *IT*-curves, which allows determination of the S/V ratio for the sample under study.

The $I(X)$ curve is given by the following expression[224]

$$I(X) = \sum_{i=1}^{N} \frac{I_0}{\sqrt{\pi}} \int_0^{(X-X_{ci})/\sqrt{2\Delta_i}} \exp(-u^2)\mathrm{d}u. \tag{17}$$

The derivative,

$$\frac{\mathrm{d}I}{\mathrm{d}X} = \sum_{i=1}^{N} \frac{I_{0i}}{\sqrt{\pi}} \exp\left(-\frac{X - X_{ci}}{\sqrt{2\Delta_i}}\right)^2 \tag{18}$$

is the sum of Gaussian functions with the transition temperatures $T_{ci} = 1/X_{ci}$, widths Δ_i and weights I_{0i}. The correlation time distribution of molecular motions is assumed to be log-normal.

Taking into account Eqn (16a), the differential pore size distribution can be represented as follows:[225]

$$\frac{\mathrm{d}I}{\mathrm{d}R} = -\frac{K}{R^2}\frac{\mathrm{d}I}{\mathrm{d}T}. \tag{19}$$

The pore sizes that can be measured using the NMR cryoporosimetry technique span the range from $\sim$10 to 2000 Å.[221–223, 225]

The *IT*-curves of water in silica were measured.[224, 225] The broad component corresponding to the largest X value ($T = 210$ K) was attributed to the phase transition at the interface between the pore surface and the rest of the solid ice within the pore.[224] Simultaneous fitting of the data obtained for samples with different pore sizes allowed one to avoid the necessity of independent determination of the parameters K and d. The silanol groups were found to contribute to the NMR signal.[225] The NMR spectrum of benzene in silica and zeolite Y (pore size 7.4 Å) at 227 K comprises several broad overlapped lines. Assuming fast proton exchange between the fluid at the pore wall and the rest of the fluid in the pore, the average chemical shift value was found to be dependent on the thickness, d, of the surface layer. Estimations from positions of the NMR signals give the same value as that obtained from analysis of the *IT*-curves. The chemical shift

appreciably changes as the pore radius R changes in the mesopore range (at $R > 10$ Å) while it remains virtually unchanged for micropores ($R < 10$ Å). This can be used for the determination of the volume fraction of micropores in the sample. The results obtained were found to be in good agreement with those found by low-temperature adsorption of nitrogen.

It is convenient to perform model experiments using the mesoporous material MCM-41 which possesses a hexagonal array of identical one-dimensional mesopores of size in the range from 18 to 100 Å. Some of the *IT*-curves of water exhibited characteristic hysteresis effects between cooling and heating processes, while the results of several cooling–heating cycles were identical, which means that the phase transition causes no mechanical damages to the pore space.[224] The *IT*-curves of MCM-41 with a pore size of 26 Å exhibited [193] a narrow phase transition at 226 K. In addition, a broad (without hysteresis) transition was observed [193, 227] in the temperature range 200–207 K, which corresponds [227] to a total of more than 60% of the overall amount of water and cannot be attributed to the fluid in micropores due to their lack. It was assumed [227] that the pore contains a layer of the fluid ~ 5 Å thick, which gradually freezes at a lower temperature compared to the rest of the fluid in the pore. This is in agreement with substantial broadening of the NMR signal on cooling due to a decrease in the molecular mobility and to enhancement of the effects associated with differences in the magnetic susceptibilities.[227]

At the same time, it is possible that the low-temperature phase transition is only an apparent transition. Mention has been made [192] that if the correlation time distribution of the molecular motions is broad, cooling can lead to observation of an apparent phase transition when performing the T_2 NMR measurements. This transition is associated with reduction of the molecular mobility and with passage from exponential relaxation to the rigid lattice regime with a Gaussian relaxation decay. Such a transition is not accompanied by changes in the phase state and is manifested only in the NMR experiments. For instance, studies of water adsorbed on silica gel and on porous glass with the pore sizes 60 to 240 Å revealed not only the phase transitions at 273 K for the excess water and at 265 K (with hysteresis) for the pore water but also an apparent transition in the temperature range 120–255 K, which occurs smoothly without hysteresis.[220] Only a water layer two or three monolayers thick is involved in the apparent transition. The corresponding distribution of correlation times is shifted towards longer times as the temperature decreases. This is accompanied by retardation of proton exchange between the molecules with different T_2 values. Studies of the samples with controlled pore filling showed that initially the amount of non-freezing water increases as the amount of adsorbed water increases and then is saturated at a level corresponding to coverage of the surface of the pore space by two or three monolayers of water. The 'non-freezing water' does not assume the structure of ice on cooling below the freezing point and differs from liquid water at high temperatures.

Combining the results of analysis of the temperature dependences of the parameters ΔT and $1/T_1$ allowed determination of the enthalpy of freezing of bound water and of the width of the correlation time distribution of water molecules.[193, 220] The ΔT and $1/T_1$ values are inversely proportional to the pore sizes; because of this, a linear correlation between ΔT and $1/T_1$ was observed [228] for water in MCM-41 with the pore sizes ranging from 19 to 38 Å at 263 K.

The results obtained for water in MCM-41 are in good agreement with the data obtained by low-temperature adsorption of nitrogen and by high resolution electron microscopy.[224] However, expression (18) cannot describe the experimental data for the microporous material (aluminophosphate molecular sieves VPI-5).

By varying the pore saturation level one can study the process of filling of porous materials with fluids. Controlled saturation (10%–100%) studies of porous silica (silica gel with 60 Å pores) with water or cyclohexane have been reported.[226] The samples were initially cooled down to 173 K (cyclohexane) or 223 K (water) and the measurements were carried out during heating. It was found that cyclohexane fills out the entire pores starting from the smallest ones, whereas water initially forms droplets whose size is much smaller than that of the smallest pores in the sample. The size of the water droplets increases as the saturation level of the sample increases. The freeze–thaw cycles have no effect on the characteristics of the pore space. The character of the relaxation time distribution of cyclohexane is such that the pore size distributions exhibit false peaks.[226] In addition, solid cyclohexane undergoes a phase transition from a monoclinic crystal structure to a plastic f.c.c. crystal at 186 K.[229] Measurements of the relaxation times T_2 and $T_{1\rho}$ in the temperature range 77–295 K for cyclohexane in silica gel with pores of size 60, 200 and 500 Å revealed a phase transition in solid cyclohexane in the two last-named samples.

Spatially resolved (1D, 2D and 3D) *IT*-curves of water and cyclohexane in porous silica of different pore sizes have been reported.[222, 223] The NMR signal was calibrated against that of isopentane which has a low freezing point. The results obtained allowed determination of the pore size distribution at any point of the sample [223] and imaging of those regions of the object that contained pores of preset sizes.[222] The relaxation time T_2 of solid cyclohexane was $\leqslant 2$ ms.

Spatially resolved NMR cryoporosimetry was used for determination of the size of filled pores in partially dried concrete prepared from white Portland cement and quartz filler.[230, 231] On cooling, freezing began at the centre of the sample (this region is characterised by larger amount of water and by filling of larger pores).[230] Further cooling led to uniform freezing of water along length of the sample. No freezing of water occurred in the gel pores even at -53 °C. The apparent phase transition in the form of a slow (without hysteresis) change in the amplitude of the NMR signal was also observed. The 1D moisture profiles of cylindrical concrete and mortar samples were obtained simultaneously and their changes were traced during cooling down to 223 K. This experiment allowed one to determine the size of the filled pores along the length of a cylindrical sample.[232] The sample completely saturated with water exhibited a phase transition at ~ 273 K corresponding to a wide range of mesopores. The samples of partially water-saturated concrete and mortar exhibited identical distributions of the filled pore sizes. It was found that most of the water resides in the pores of size less than 6 nm. Characteristic of all samples was a dramatic decrease in the NMR signal amplitude at ~ 223 K. This is associated with desorption of water followed by the formation of ice in another regions of the sample. At 218 K, nearly 50%–55% of water exists in the form of ice. The relaxation times (T_1, T_2 and T_2^*) were mapped and it was shown that the times T_2 and T_2^* are shortened while the time T_1 is lengthened as temperature decreases.

* * *

The features of NMR image contrast formation allows the use of the NMR imaging technique for obtaining a vast variety of information on the objects under study. The authors of this review tried to emphasise some salient features and to illustrate potential applications of this method. Additional information on the studies of the structure and properties of liquid-containing materials is presented in the Supplement.

This work has been written with the financial support of the Russian Foundation for Basic Research (Project Nos 02-03-32770 and 00-15-97450) and the Siberian Branch of the Russian Academy of Sciences (the 'Integration' Programme Project No. 46).

V. Supplement

Additional information on the studies of the structure and properties of liquid-containing materials is given in Table S.1.

Table S.1. Applications of the MRI technique based on the ^{1}H NMR signals.

Magnetic field /T	Object, process	Technique	Dimension	Spatial resolution characteristics [a]	Recording time	Ref.
1.4	Water + 0.1% $CuSO_4$ in a pipe with abrupt contraction (expansion)	spin echo + PRI	2D	64×64, a slice 0.33 mm thick	–	19
0.73	Plastic or rubber articles	gradient echo with oscillating gradients	3D	$64 \times 64 \times 64$, $(0.5\ mm)^3$	3 h 38 min	26
4.7	Vulcanised rubber impregnated with aluminium and sodium sulfate crystals; filled phenol-formaldehyde resin; a 72-h *Manduca sexta* caterpillar	spin echo or PRI	2D	180° FIDs, $(35\ \mu m)^2$ for PRI 128×128, a slice 1 mm thick or without slice selection	from 2 to 17 h	27
0.7	Sandwich-type layered model sample; alkyd resin film coated with cobalt catalyst	spin echo	1D	256, 512; 13, 6.5 μm	17 min	83
0.4	Various solid materials	the same	–	WSR	–	84
2.0	Water in Al_2O_3, water + NaCl in sandstone rock or limestone rock cores	"	2D, 3D	128×128, $(200\ \mu m)^2$, a slice 5 mm thick (2D); $128 \times 128 \times 256$, $(300\ \mu m)^3$ (3D)		86
0.1	Water in sandstone rock plugs	"	1D, 3D	1 mm (1D); $2.4 \times 2.4 \times 7$ mm (3D)	3 min (1D); 1 h (3D)	90
2.0	Oil + water or brine in dolomite plugs	–	2D	–	–	92
4.7	H_2O/D_2O or H_2O/hydrocarbon mixture in limestone rock sample	spin echo	2D	128×128, $(0.94\ mm)^2$, a slice 5 mm thick	35 min	94
1.9	Water or n-dodecane in sandstone rock cores	the same	2D	256×256	–	95
2.0	Aqueous KCl solution and dodecane in sandstone rock core	"	2D	128×128, $(0.44\ mm)^2$, a slice 5 mm thick	43 min	96
2.0	Water, sunflower oil or sunflower oil-in-water emulsion flowing in a pipe	gradient echo	2D, 3D	64×64, $(850\ \mu m)^2$, $(780\ \mu m)^2$, a slice 2 mm or 2.5 mm thick (2D); $64 \times 64 \times 64$, $(710\ \mu m)^3$ (3D)	20 – 60 s (2D); 23 min (3D)	97
0.5	Decane in peroxide vulcanised natural rubber	gradient echo with oscillating field gradients	2D	250 (400) μm for decane, 600 μm for rubber, a slice 5 mm thick	20 min	98, 99
1.89	Water or motor oil/H_2O/D_2O mixture in sandstone rock sample	spin echo with inversion – recovery	3D	$256 \times 256 \times 256$, $20 \times 19 \times 930$ μm	–	100
2.0	Water + salt and petroleum in chalk core	–	2D	$(800\ \mu m)^2$, a slice 3 or 5 mm thick	–	101
2.0	Acetone + benzene in vulcanised rubber cylinder	chemical shift selective spin echo	2D	a slice 4 mm thick	2 min	102
2.0	Isooctane in vulcanised rubber cylinder saturated with cyclohexane	gradient echo for two-quantum coherence	2D	a slice 8 mm thick	8 min	102
	Salt solution in sandstone rock sample	–	2M	–	–	103
4.7	LiCl brine or trifluorotoluene in sandstone rock samples [b]	–	3D	$64 \times 64 \times 16$, $1 \times 1 \times 5$ mm (^{7}Li); $128 \times 128 \times 16$, $0.4 \times 0.4 \times 3$ mm (^{1}H, ^{19}F)	546 min (^{7}Li); 273 min (^{19}F); 17 min (water); 273 min (^{1}H of trifluorotoluene)	104
1.5, 4.7	Water in porous glass disk-shaped pellets	spin echo or gradient echo	2D, 3D	256×128, 128×128, $(0.1 – 1\ mm)^2$, a slice 80 μm to 3 mm thick (2D)	from 4 min to 9 h	105
9.4	Methane in zirconia bead pack	FID or spin echo	–	WSR	–	107

Table S.1 (continued).

Magnetic field /T	Object, process	Technique	Dimension	Spatial resolution characteristics [a]	Recording time	Ref.
2.0	Alumina powder compacts prepared with polymeric binder	spin echo	2D	128×128, $(552\ \mu m)^2$, 64×64, $(652\ \mu m)^2$, 128×128, $(326\ \mu m)^2$	from 3.5 to 28 min	108
0.47	Aqueous $MnCl_2$ solution (1.5 – 25 mM), water in plant tissues	the same	2D	128×128, $(0.23\ mm)^2$, 256×256, $(0.1\ mm)^2$, a slice 2 or 5 mm thick	–	109
4.7	Water in alumina or silica	"	2D	128×128, $(40\ \mu m)^2$, a slice 0.3 to 1 mm thick	–	110
7.05, 9.4	Water + ethanol in alumina granules	"	2D, 3D	256×256, $(39\ \mu m)^2$, a slice 200 μm thick; $128 \times 128 \times 128$ (3D)	30 min (2D)	111
2.0	Water in alumina, salt solution in sandstone rock samples	"	2D	128×128, $(0.5\ mm)^2$, a slice 5 mm thick	2.5 h	112
4.7	Water in alumina or silica	stimulated echo	–	WSR	–	113
		spin echo or gradient echo	2D	128×128, 64×64, $(30 – 100\ \mu m)^2$, a slice 0.2 to 1 mm thick	< 30 min	114
4.7	Water or H_2O/D_2O mixture in alumina or silica	the same	2D	128×128, 64×64, $(30 – 190\ \mu m)^2$, a slice 0.2 to 1 mm thick	1.7 or 3.4 min	115
4.7	H_2O/D_2O mixture in alumina	spin echo	1D, 2D	128×128, $(100\ \mu m)^2$, a slice 1 mm thick (2D)	40 s (1D), 3.4 min (2D)	116
4.7	Water or H_2O/D_2O mixture in alumina or silica	the same	2D	128×128, $(40\ \mu m)^2$, a slice 0.3 to 1 mm thick	–	117
4.7	Water or H_2O/D_2O mixture in alumina or silica gel	"	2D	128×128, $(40\ \mu m)^2$,	–	120
7.05	Cyclohexane or aniline + cyclohexane in glass filter	"	1D	2048; 26 μm	–	121
4.7	Water in glass bead pack	spin echo (EPI or PEPI)	2D, 3D	128×128, $(94\ \mu m)^2$, a slice 0.5 mm thick (2D); $128 \times 128 \times 128$, $(117\ \mu m)^3$ (3D)	51 min or 24 s (2D); 9 h or 15 min (3D)	122
–	Water in latex microsphere bead pack	spin echo	2D	128×128, $(31.5\ \mu m)^2$, a slice 200 μm thick 64×64, $(63.5\ \mu m)^2$, a slice 1 mm thick	–	125
–	Water in porous polystyrene, natural sponge, pumice stone or glass bead pack	spin echo or gradient echo	3D	–	–	128
4.7	Water in alumina pellets with coke	gradient echo	2D	128×128, $(40\ \mu m)^2$, a slice 0.5 mm thick	4 h	129
7.05, 9.4	Benzene (+ Xe) in zeolite powder; 2,3-dimethylpentane or Xe in zeolite pellets with coke [c]	spin echo	1D, 2D	–	–	130
0.84	Aqueous NaCl solution in sandstone rock samples	spin echo + PRI	2D	256×256, a slice 1.5 cm thick	5 min	135
0.5	Water or 3% aqueous NaCl solution in dolomite, sandstone rock and petroleum well plug	spin echo (PEPI)	2D, 3D	$64 \times 64 \times 128$, $(1.5\ mm)^3$	1.5 min	136
7.05	Vulcanised *cis*-1,4-polybutadiene + cyclohexane-d_{12}	spin echo	2D	256×256, $(37\ \mu m)^2$, $(58\ \mu m)^2$, a slice 1 mm thick	–	139
7.05	Vulcanised polybutadiene rubber + deuterocyclohexane or cyclohexane-d_{12}	the same	2D	256×256, $(39\ \mu m)^2$, $(32\ \mu m)^2$	–	140
2.0	Water in a polymeric composite reinforced with carbon fibre		3D	$256 \times 256 \times 16$, $0.25 \times 0.25 \times 7$ mm	2.5 h	141

Table S.1 (continued).

Magnetic field /T	Object, process	Technique	Dimension	Spatial resolution characteristics [a]	Recording time	Ref.
7.05	Cyclohexane in cross-linked *cis*-1,4-polyisoprene + triaryl cyanurate + zinc diacrylate	spin echo	2D	256 × 256, $(78\ \mu m)^2$, a slice 1 mm thick	–	142
7.05	Water + poly-*N*-isopropylacrylamide gel	the same	1D, 2D	a slice 1 mm thick	–	143
6.34	Water or water + $MnSO_4$ mixture in cross-linked polymethacrylic acid gel	"	2D	a slice 2 mm thick		144, 145, 146
2.35	Sodium alginate + NaCl + water, dialysis against aqueous $CaCl_2$ solution	"	2D	256×128 $(135\ \mu m)^2$, a slice 3 mm thick		147
0.47	Agar gel	"	–	WSR	–	148
2.35	Agar gel doped with Mn(II), mortar, concrete, polyethylene	SPRITE	2D	64×64, $(1.25-1.5\ mm)^2$	–	149
1.0	Aqueous Al_2O_3 + $CuSO_4$ suspension in plaster of Paris mould	spin echo	2D	128×128, $(200\ \mu m)^2$, a slice 8 mm thick	64 s	150
	Organic components in Si_3N_4 or Al_2O_3	the same	2D	128×128, $(640\ \mu m)^2$ $310 \times 340\ \mu m$	29 min 17 h	151
2.0	Aluminosilicate mixture + triethanolamine or tetraethylammonium bromide in batch mixer	"	2D	128×128, $(470\ \mu m)^2$, a slice 2 mm or 4 mm thick	–	152
7.05	Emulsion explosives	"	2D	128×128 $(63\ \mu m)^2$, a slice 3 mm thick	–	153
5.3	Emulsion of sunflower oil in D_2O	STRAFI	1D	–	1, 7 min	154
0.35	Water in food systems	SPRITE, spin echo	1D, 2D; 2D	64×64 (2D)	4 min, 15 min	155
2.35, 4.7	Apple	spin echo	2D	128×128, a slice 2 mm thick	–	156
–	Apple, peach	the same	2D	128×128 $(0.78\ mm)^2$, 64×64 $(1.56\ mm)^2$, a slice 5 mm thick	0.9 s	157
0.5	Watermelon	"	1D, 2D	256, a slice 20 mm thick (1D)	–	158
7.05	Tomato	"	2D	128×128 $(0.2\ mm)^2$, a slice 1 mm thick	–	159
4.7 2.4	Cigarettes	spin echo, SPI, SPRITE	1D, 2D, 3D	32×32, $(300\ \mu m)^2$	–	160
0.5	White oak or black cherry logs	spin echo	2D	$(1.2\ mm)^2$, $(1.95\ mm)^2$	7.5 min	161
9.45	Coal or coal + pyridine-d_5	SPI, spin echo	2D, 3D	128×128, $(50\ \mu m)^2$ (2D); $128 \times 128 \times 128$, $(50\ \mu m)^3$ (3D)	8 min (2D); 16 h (3D)	164
9.4	Water inside the CD_4 + ice gas hydrate	spin echo	2D	128×128 $(80\ \mu m)^2$, a slice 0.5 mm thick	–	165
4.3	Xe (80% ^{129}Xe) (1 – 3 atm) in nested tubes or capillary bundle [d]	gradient echo (FLASH)	2D	128×64, 0.1 mm	–	168
4.3	Xe (80% ^{129}Xe) (1 – 3 atm) in aerogel [d]	the same	1D	0.1 mm	–	168
9.4	Xe (70% ^{129}Xe) in mice lungs *in vitro* (in ampoule) [d]	"	2D	128×128, $(0.37\ mm)^2$	600 ms	169
2.0	Foam churned from egg white and water	spin echo	1D	–	–	172
1.89	Foam churned from water with surfactant, polymer and alcohol additives	the same	1D	–	–	173
2.0	Salt solution in sandstone rock or limestone rock samples	stimulated echo	–	WSR	7 h	174

Table S.1 (continued).

Magnetic field /T	Object, process	Technique	Dimension	Spatial resolution characteristics [a]	Recording time	Ref.
1.9	C_2F_6 or C_4F_8 in ceramics (Y-stabilised zirconia) [c]	spin echo	3D	–	2 h	175
2.0	Water in a gap between glass plates	the same	–	WSR	–	176
178	Various liquids in rock or alumina samples	stimulated echo	–	"	–	
7.05	Acetonitrile, benzene, dichloromethane and CCl_4 in carbonaceous adsorbent	FID	–	"	–	180
0.7	Water in porous glass	"	–	"	–	191
7.05	Water in MCM-41	"	–	"	–	193
0.23	Water in calcium carbonate packs in the presence of Mn, Fe or Co ions	–	–	"	–	195
0.05	Water in calcium silicate packs in the presence of Mn or Fe ions	spin echo	–	"	7 min, 2 h	196
2.0	Water in sandstone rock samples	–	1D	"	–	200
0.47	Water or cyclohexane in silica	spin echo	–	WSR	–	202
2.0	Bentonite + water + NaOH + lignosulfonate dispersant (+ barite) in sandstone rock or limestone rock cores	the same	1D	128	–	203
7.05, 0.55	Acetone in corn starch gel	"	–	WSR	–	205
0.7	Water in sandstone rock plugs	FID, gradient echo or spin echo	1D	WSR, 0.2 mm	–	206
2.0	Water in glass bead pack or in limestone rock, chalk or sandstone rock samples	inversion – recovery, stimulated echo	–	WSR	–	207
1.0	3% Aqueous NaCl solution in sandstone rock or limestone rock cores	FID	–	"	45 – 60 min	209
0.66, 2.35	Aqueous salt solution, dodecane or cyclooctane in sandstone rock and carbonate rock plugs	FID, spin echo	–	"	–	210
0.78	Water in crushed porous glass	the same	–	"	–	214
2.1	Water in silica gel, porous glass, activated charcoal	FID	–	"	–	220
7.05	Water in silica (amorphous silicate)	the same	–	"	–	221
0.5, 2.5	Water or cyclohexane in porous silica	spin echo	1D, 2D, 3D	64×64 (2D), $64 \times 64 \times 32$ (3D)	4.3 min (2D), 1 h (3D)	222
0.5, 2.5	The same	the same	1D, 2D, 3D	64×64, a slice 20 mm thick (2D); $64 \times 64 \times 32$ (3D)	4.3 min (2D); 60 min (3D)	223
7.05	Water in MCM-41, aluminophosphate molecular sieves (VPI-5) and amorphous silicate	FID	–	WSR	–	224
7.05	Water, benzene, cyclohexane in porous silica	spin echo or FID	–	"	–	225
	Water, cyclohexane in porous silica	spin echo	–	"	–	226
7.05	Water in MCM-41, silica, zeolite Y and industrial catalyst	FID	–	"	–	227
7.05	Water in MCM-41	"	–	"	–	228
0.5	Cyclohexane in porous silica	FID or spin echo	–	"	–	229

Table S.1 (continued).

Magnetic field /T	Object, process	Technique	Dimension	Spatial resolution characteristics [a]	Recording time	Ref.
2.35	Water in concrete (white Portland cement + quartz filler)	SPRITE	1D	64; 1.6 mm	–	230
2.4	Water in mortar or concrete	"	1D	64; 2.2 mm		231, 232

Notations: PRI is Projection Reconstructed Imaging, WSR is Without Spatial Resolution, FID is Free Induction Decay, EPI is Echo-Phanar Imaging, PEPI is Echo-Planar Imaging with Pi-pulses; STRAFI is Stray Field Imaging and FLASH is Fast Low-Angle Shot.
[a] Listed are the image dimension (in pixels), spatial resolution and slice thickness. [b] Imaging using the ^{1}H, ^{7}Li and ^{19}F NMR signals. [c] Imaging using the ^{1}H and ^{129}Xe NMR signals. [d] Imaging using the ^{129}Xe NMR signals. [e] Imaging using the ^{19}F NMR signals.

References

1. W Kuhn *Angew. Chem., Int. Ed.* **29** 1 (1990)
2. S L Talagala, I J Lowe *Concepts Magn. Reson.* **3** 145 (1991)
3. J P Hornak *Osnovy MRT*, 1996 – 1999) (The Basics of NMR, 1996 – 1999); http://www.cis.rit.edu/htbooks/mri/inside-r.thm
4. A C Kak, M Slaney *Principles of Computerized Tomographic Imaging* (IEEE Press, 1988); http://www.slaney.org/pct/pct-toc.html
5. E Zavoiskii *Zh. Fiziki* **9** 245 (1945)
6. F Bloch, W W Hansen, M Packard *Phys. Rev.* **69** 127 (1946)
7. E M Purcell, H C Torrey, R V Pound *Phys. Rev.* **69** 37 (1946)
8. E L Hahn *Phys. Rev.* **80** 580 (1950)
9. R R Ernst, W A Anderson *Rev. Sci. Instrum.* **37** 93 (1966)
10. T C Farrar, E D Becker *Pulse and Fourier Transform NMR* (New York; London: Academic Press, 1971)
11. A E Derome *Modern NMR Techniques for Chemistry Research* (Oxford: Pergamon Press, 1987)
12. J P Hornak *The Basics of NMR, 1996 – 2002*; http://www.cis.rit.edu/htbooks/mri/inside.htm
13. R R Ernst, G Bodenhausen, A Wokaun *Principles of Nuclear Magnetic Resonance in One and Two Dimensions* (Oxford: Clarendon Press, 1987)
14. A Bax *Two-Dimensional Nuclear Magnetic Resonance in Liquids* (Delft: Delft University Press, 1982)
15. H Kessler, M Gehrke, C Griesinger *Angew. Chem., Int. Ed.* **27** 490 (1988)
16. R R Ernst *Angew. Chem., Int. Ed.* **31** 805 (1992)
17. A Kumar, D Welti, R R Ernst *J. Magn. Reson.* **18** 69 (1975)
18. P C Lauterbur *Nature (London)* **242** 190 (1973)
19. Y Xia, P T Callaghan, K R Jeffrey *AIChE J.* **38** 1408 (1992)
20. T Hou, J Smith, E MacNamara, M Macnaughtan, D Raftery *Anal. Chem.* **73** 2541 (2001)
21. *Chem. Eng. Sci.* (*Special Issue on Process Tomography*) **52** 13 (1997)
22. J-M Nuzillard, R Freeman *J. Magn. Reson. A* **107** 113 (1994)
23. E Kupce, R Freeman *J. Magn. Reson. A* **112** 134 (1995)
24. S McDonald, W S Warren *Concepts Magn. Reson.* **3** 55 (1991)
25. P T Callaghan *Principles of Nuclear Magnetic Resonance Microscopy* (Oxford: Clarendon Press, 1991)
26. M J D Mallett, S L Codd, M R Halse, T A P Green, J H Strange *J. Magn. Reson. A* **119** 105 (1996)
27. J M Listerud, S W Sinton, G P Drobny *Anal. Chem.* **61** 23A (1989)
28. G T Herman *Image Reconstruction from Projections. Implementation and Applications* (Berlin: Springer, 1979)
29. J C Sharp, R W Bowtell, P Mansfield *Magn. Reson. Med.* **29** 407 (1993)
30. S Choi, X-W Tang, D G Cory *Int. J. Imaging Syst. Technol.* **8** 263 (1997)
31. S Gravina, D G Cory *J. Magn. Reson. B* **104** 53 (1994)
32. B J Balcom, R P MacGregor, S D Beyea, D P Green, R L Armstrong, T W Bremner *J. Magn. Reson. A* **123** 131 (1996)
33. I V Mastikhin, B J Balcom, P J Prado, C B Kennedy *J. Magn. Reson.* **136** 159 (1999)
34. C B Kennedy, B J Balcom, I V Mastikhin *Can. J. Chem.* **76** 1753 (1998)
35. B J Balcom, in *Spatially Resolved Magnetic Resonance. Methods, Materials, Medicine, Biology, Rheology, Geology, Ecology, Hardware* (Eds B Blümich, P.Blümler, R Botto, E Fukushima) (Weinheim: Wiley-VCH, 1998)
36. J Hennig, A Nauerth, H Friedburg *Magn. Reson. Med.* **3** 823 (1986)
37. J Hennig *J. Magn. Reson.* **78** 397 (1988)
38. A Haase, J Frahm, D Matthaei, W Haenicke, K-D Merboldt *J. Magn. Reson.* **67** 258 (1986)
39. A Haase *Magn. Reson. Med.* **13** 77 (1990)
40. M T Vlaardingerbroek, J A den Boer *Magnetic Resonance Imaging* (Berlin: Springer, 1996)
41. P Mansfield, A M Blamire, R Coxon, P Gibbs, D N Guilfoyle, P Harvey, M Symms *Philos. Trans. R. Soc. London A* **333** 495 (1990)
42. R Mulkern *Concepts Magn. Reson.* **4** 307 (1992)
43. D Yang, T Kodama, S Tamura, K Watanabe *Magn. Reson. Imaging* **17** 171 (1999)
44. T Scaeffter, V Rasche, P Bornert, G Mens *Magn. Reson. Imaging* **19** 677 (2001)
45. N G Papadakis, A A Wilkinson, T A Carpenter, L D Hall *Magn. Reson. Imaging* **15** 567 (1997)
46. A A Savelov, R Z Sagdeev *Med. Fiz.* (11) 108 (2001)
47. F O Zelaya, W U Roffmann, S Crozier, S Teed, D Gross, D M Doddrell *Magn. Reson. Imaging* **15** 497 (1997)
48. A A Maudsley, H E Simon, S K Hilal *J. Phys. E* **17** 216 (1984)
49. D Tomasi, H Panepucci, E L Vidoto, E R Azevedo *J. Magn. Reson.* **131** 310 (1998)
50. D Tomasi, H Panepucci *Magn. Reson. Imaging* **17** 157 (1999)
51. G N Chmurny, D I Hoult *Concepts Magn. Reson.* **2** 131 (1990)
52. B J Balcom, M Bogdan, R L Armstrong *J. Magn. Reson. A* **118** 122 (1996)
53. R E Wysong, I J Lowe *Magn. Reson. Med.* **29** 119 (1993)
54. M Terpstra, P M Andersen, R Gruetter *J. Magn. Reson.* **131** 139 (1998)
55. I Sersa, O Jarh, F Demsar *J. Magn. Reson. A* **111** 93 (1994)
56. G C Scott, M L G Joy, R L Armstrong, R M Henkelman *J. Magn. Reson.* **97** 235 (1992)
57. G C Scott, M L G Joy, R L Armstrong, R M Henkelman *Magn. Reson. Med.* **28** 186 (1992)
58. P Maffei, P Mutzenhardt, A Retournard, B Diter, R Raulet, J Brondeau, D Canet *J. Magn. Reson. A* **107** 40 (1994)
59. K K Woelk, J W Rathke, R J Klinger *J. Magn. Reson. A* **109** 137 (1994)
60. R Raulet, J-M Escanye, F Humbert, D Canet *J. Magn. Reson. A* **119** 111 (1996)
61. D V Trushkin, O A Shushakov, A V Legchenko *Appl. Magn. Reson.* **5** 399 (1993)
62. R Kimmich, B Simon, H Kostler *J. Magn. Reson. A* **112** 7 (1995)
63. K Woelk, R E Gerald II, R J Klinger, J W Rathke *J. Magn. Reson. A* **121** 74 (1996)
64. B Blumich *Concepts Magn. Reson.* **10** 19 (1998)
65. B Blumich, P Blumler, L Gasper, A Guthausen, V Gobbels, S Laukemper-Ostendorf, K Unseld, G Zimmer *Macromol. Symp.* **141** 83 (1999)
66. P Blumler, B Blumich *NMR Basic Princip. Prog.* **30** 209 (1994)
67. P Blumler, B Blumich *Rubber Chem. Technol.* **70** 468 (1997)

68. P Jezzard, J J Attard, T A Carpenter, L D Hall *Prog. NMR Spectr.* **23** 1 (1991)
69. J B Miller *Prog. NMR Spectr.* **33** 273 (1998)
70. S-C Lee, K Kim, J Kim, S Lee, J H Yi, S W Kim, K-S Ha, C Cheong *J. Magn. Reson.* **150** 207 (2001)
71. R Verhagen, A Wittlin, C W Hilbers, H van Kempen, A P M Kentgens *J. Am. Chem. Soc.* **124** 1588 (2002)
72. K Wago, D Botkin, C S Yannoni, D Rugar *Appl. Phys. Lett.* **72** 2757 (1998)
73. D Rugar, C S Yannoni, J A Sidles *Nature (London)* **360** 563 (1992)
74. D Rugar, O Zuger, C S Hoen, S Yannoni, H-M Vieth, R Kendrick *Science* **264** 1560 (1994)
75. S Singh, R Deslauriers *Concepts Magn. Reson.* **7** 1 (1993)
76. I Sersa, S Macura *J. Magn. Reson.* **143** 208 (2000)
77. I Sersa, S Macura *J. Magn. Reson. B* **111** 186 (1996)
78. I Sersa, S Macura *J. Magn. Reson.* **135** 466 (1998)
79. I Sersa, S Macura *Int. J. Imag. Syst. Technol.* **10** 225 (1999)
80. S W Gould, A Darzi *Br. J. Radiol.* **70** S89 (1997)
81. S Gould, A Darzi *Br. J. Surgery* **84** 595 (1997)
82. G M Lamb, M G de Jode, S W Gould, E Spouse, K Birnie, A Darzi, W M W Gedroyc *Br. J. Radiol.* **73** 152 (2000)
83. P M Glover, P S Aptaker, J R Bowler, E Ciampi, P J McDonald *J. Magn. Reson.* **139** 90 (1999)
84. G Eidmann, R Savelsberg, P Blumler, B Blumich *J. Magn. Reson. A* **122** 104 (1996)
85. C T W Moonen, P A Bandettini (Eds) *Functional MRI* (Heidelberg: Springer, 1999)
86. P A Osment, K J Packer, M J Taylor, J J Attard, T A Carpenter, L D Hall, N J Herrod, S J Doran *Philos. Trans. R. Soc. London A* **333** 441 (1990)
87. S Chen, X Yao, J Qiao, A T Watson *Magn. Reson. Imaging* **13** 599 (1995)
88. B Issa, P Mansfield *Magn. Reson. Imaging* **12** 213 (1994)
89. J J Howard *Magn. Reson. Imaging* **12** 197 (1994)
90. G Guillot, C Chardaire-Riviere, S Bobroff, A Le Roux, J C Roussel, L Cuiec *Magn. Reson. Imaging* **12** 365 (1994)
91. L D Hall, S Sukumar, S L Talagala *J. Magn. Reson.* **56** 275 (1984)
92. G C Borgia, A Brancolini, A Camanzi, G Maddinelli *Magn. Reson. Imaging* **12** 221 (1994)
93. L D Hall, S Sukumar *J. Magn. Reson.* **56** 314 (1984)
94. J M Dereppe, C Moreaux, K Schenker *J. Magn. Reson.* **91** 596 (1991)
95. L D Hall, V Rajanayagam, C Hall *J. Magn. Reson.* **68** 185 (1986)
96. M A Horsfield, C Hall, L D Hall *J. Magn. Reson.* **87** 319 (1990)
97. B Newling, S J Gibbs, L D Hall, D E Haycock, W J Frith, S Ablett *Chem. Eng. Sci.* **52** 2059 (1997)
98. M R Halse, H J Rahman, J H Strange *Physica B* **203** 169 (1994)
99. M R Halse *Magn. Reson. Imaging* **14** 745 (1996)
100. L D Hall, V Rajanayagam *J. Magn. Reson.* **74** 139 (1987)
101. S Davies, A Hardwick, D Roberts, K Spowage, K J Packer *Magn. Reson. Imaging* **12** 349 (1994)
102. A G Webb, L D Hall *Polym. Commun.* **31** 425 (1990)
103. H J Vinegar *J. Petrol. Technol.* **38** 257 (1986)
104. S N Sarkar, J J Dechter, R A Komoroski *J. Magn. Reson. A* **102** 314 (1993)
105. S N Sarkar, E W Wooten, R A Komoroski *Appl. Spectrosc.* **45** 619 (1991)
106. H Van As, D van Dusschoten *Geoderma* **80** 389 (1997)
107. M E Smith, S N Stuart *J. Phys. D* **28** 229 (1995)
108. L Garrido, J L Ackerman, W A Ellingson *J. Magn. Reson.* **88** 340 (1990)
109. H T Edzes, D van Dusschoten, H Van As *Magn. Reson. Imaging* **16** 185 (1998)
110. S Rigby *J. Colloid Interface Sci.* **224** 382 (2000)
111. A Timonen, L Alvila, P Hirva, T T Pakkanen, D Gross, V Lehmann *Appl. Catal. A* **129** 117 (1995)
112. J J Attard, T A Carpenter, L D Hall, S Davies, M J Taylor, K J Packer *Magn. Reson. Imaging* **9** 815 (1991)
113. M P Hollewand, L F Gladden *Chem. Engng Sci.* **50** 309 (1995)
114. M P Hollewand, L F Gladden *J. Catal.* **144** 254 (1993)
115. M P Hollewand, L F Gladden *Chem. Eng. Sci.* **50** 327 (1995)
116. S P Rigby, K-Y Cheah, L F Gladden *Appl. Catal. A* **144** 377 (1996)
117. S P Rigby, L F Gladden *J. Catal.* **173** 484 (1998)
118. E O Stejskal, J E Tanner *J. Chem. Phys.* **42** 288 (1965)
119. J Karger, D M Ruthven *Diffusion in Zeolites and other Microporous Solids* (New York: Wiley, 1992)
120. S P Rigby, L F Gladden *Chem. Engng Sci.* **54** 3503 (1999)
121. L Tremblay, S Lacelle, C G Fry *Can. J. Chem.* **76** 1633 (1998)
122. B Manz, P S Chow, L F Gladden *J. Magn. Reson.* **136** 226 (1999)
123. S Sharma, M D Mantle, L F Gladden, J M Winterbottom *Chem. Eng. Sci.* **56** 587 (2001)
124. E Fukushima *Annu. Rev. Fluid Mech.* **31** 95 (1999)
125. J D Seymour, P T Callaghan *AIChE J.* **43** 2096 (1997)
126. J M Pope, S Yao *Concepts Magn. Reson.* **5** 281 (1993)
127. A Caprihan, E Fukushima *Phys. Rep.* **198** 195 (1990)
128. A Klemm, H-P Muller, R Kimmich *Physica A* **266** 242 (1999)
129. K Y Cheah, N Chiaranussati, M P Hollewand, L F Gladden *Appl. Catal. A* **115** 147 (1994)
130. J-L Bonardet, T Domeniconi, P N'Gokoli-Kekele, M-A Springuel-Huet, J Fraissard *Langmuir* **15** 5836 (1999)
131. B Boddenberg, B Beerwerth *J. Phys. Chem.* **93** 1440 (1989)
132. L Yu Khitrina, I V Koptyug, N A Pakhomov, R Z Sagdeev, V N Parmon *J. Phys. Chem. B* **104** 1966 (2000)
133. I V Koptyug, L Yu Il'ina, A V Matveev, V N Parmon, R Z Sagdeev *Khim. Fiz.* **21** 68 (2002) [a]
134. I V Koptyug, L Yu Khitrina, V N Parmon, R Z Sagdeev *Magn. Reson. Imaging* **19** 531 (2001)
135. W P Rothwell, H J Vinegar *Appl. Opt.* **24** 3969 (1985)
136. D N Guilfoyle, B Issa, P Mansfield *J. Magn. Reson. A* **119** 151 (1996)
137. A V Legchenko, O A Shushakov *Geophysics* **63** 75 (1998)
138. O A Shushakov, A V Legchenko. *Geolog. Geofiz.* **35** 140 (1994)
139. S R Smith, J L Koenig *Macromolecules* **24** 3496 (1991)
140. M A Rana, J L Koenig *Macromolecules* **27** 3727 (1994)
141. P Jackson, J A Barnes, N J Clayden, T A Carpenter, L D Hall, P Jezzard *J. Mater. Sci. Lett.* **9** 1165 (1990)
142. S J Oh, J L Koenig *Polymer* **40** 4703 (1999)
143. S Ganapathy, P R Rajamohanan, M V Badiger, A B Mandhare, R A Mashelkar *Polymer* **41** 4543 (2000)
144. H Yasunaga, H Kurosu, I Ando *Macromolecules* **25** 6505 (1992)
145. T Shibuya, H Yasunaga, H Kurosu, I Ando *Macromolecules* **28** 4377 (1995)
146. A Yamazaki, Y Hotta, H Kurosu, I Ando *J. Mol. Struct.* **554** 47 (2000)
147. A Degrassi, R Toffanin, S Paoletti, L D Hall *Carbohydr. Res.* **306** 19 (1998)
148. P S Belton, B P Hills, E R Raimbaud *Mol. Phys.* **63** 825 (1988)
149. S D Beyea, B J Balcom, P J Prado, A R Cross, C B Kennedy, R L Armstrong, T W Bremner *J. Magn. Reson.* **135** 156 (1998)
150. K Hayashi, K Kawashima, K Kose, T Inouye *J. Phys. D* **21** 1037 (1988)
151. W A Ellingson, P S Wong, S L Dieckman, J L Ackerman, L Garrido *Ceram. Bull.* **68** 1180 (1989)
152. E N Coker, P S Hees, C H Sotak, A G Dixon, R W Thompson, A Sacco *Microporous Mater.* **3** 623 (1995)
153. V M Rao, P K Ghosh *Langmuir* **16** 2985 (2000)
154. B Newling, P M Glover, J L Keddie, D M Lane, P J McDonald *Langmuir* **13** 3621 (1997)
155. P Cornillon, L C Salim *Magn. Reson. Imaging* **18** 335 (2000)
156. J Lian, D S Williams, I J Lowe *J. Magn. Reson.* **106** 65 (1994)
157. P Barreiro, C Ortiz, M Ruiz-Altsent, J Ruiz-Cabello, M E Fernandez-Valle, I Recasens, M Asensio *Magn. Reson. Imaging* **18** 1175 (2000)
158. K Saito, T Miki, S Hayashi, H Kajikawa, M Shimada, Y Kawate, T Nishizawa, D Ikegaya, N Kimura, K Takabatake, N Sugiura, M Suzuki *Cryogenics* **36** 1027 (1996)
159. Y Iwahashi, A K Horigane, K Yoza, T Nagata, H Hosoda *Magn. Reson. Imaging* **17** 767 (1999)
160. D E Axelson, J B Wooten *J. Agric. Food Chem.* **48** 2199 (2000)
161. S J Chang, J R Olson, P C Wang *Forest Prod. J.* **39** 43 (1989)
162. P A Bottomley, H H Rogers, T H Forster *Proc. Natl. Acad. Sci. USA* **83** 87 (1986)
163. D P Brown, T P Pratum, C Bledsoe, E D Ford, J S Cothern, D Perry *Can. J. Forest Res.* **21** 1559 (1991)
164. K Saito, I Komaki, K-I Hasegawa, H Tsuno *Fuel* **79** 405 (2000)
165. I L Moudrakovski, C I Ratcliffe, G E McLaurin, B Simard, J A Ripmeester *J. Phys. Chem. A* **103** 4969 (1999)

166. L A Stern, S H Kirby, W B Durham *J. Phys. Chem. A* **105** 1223 (2001)
167. W Happer, E Miron, S Schaefer, D Schreiber, W A van Wijngaarden, X Zeng *Phys. Rev. A* **29** 3092 (1984)
168. Y-Q Song, H C Gaede, T Pietrass, G A Barrall, G C Chingas, G C Ayers, A Pines *J. Magn. Reson. A* **115** 127 (1995)
169. M S Albert, G D Cates, B Driehuys, W Happer, B Saam, C S Springer, A Wishnia *Nature (London)* **370** 199 (1994)
170. M S Albert, D Balamore *Nucl. Instrum. Methods Phys. Res. A* **402** 441 (1998)
171. T Pietrass, H C Gaede, A Bifone, A Pines, J A Ripmeester *J. Am. Chem. Soc.* **117** 7520 (1995)
172. M J McCarthy *AIChE J.* **36** 287 (1990)
173. R A Assink, A Caprihan, E Fukushima *AIChE J.* **34** 2077 (1988)
174. M D Hurlimann, K G Helmer, L L Latour, C H Sotak *J. Magn. Reson. A* **111** 169 (1994)
175. A Caprihan, C F M Clewett, D O Kuethe, E Fukushima, S J Glass *Magn. Reson. Imaging* **19** 311 (2001)
176. M D Hurlimann, K G Helmer, T M de Swiet, P N Sen, C H Sotak *J. Magn. Reson. A* **113** 260 (1995)
177. P T Callaghan, D MacGowan, K J Packer, F O Zelaya *J. Magn. Reson.* **90** 177 (1990)
178. P Callaghan, D MacGowan, K J Packer, F O Zelaya *Magn. Reson. Imaging* **9** 663 (1991)
179. L Z Wang, A Caprihan, E Fukushima *J. Magn. Reson. A* **117** 209 (1995)
180. R S Drago, D C Ferris, D S Burns *J. Am. Chem. Soc.* **117** 6914 (1995)
181. M-A Springuel-Huet, J-L Bonardet, J Fraissard *Appl. Magn. Reson.* **8** 427 (1995)
182. J A Ripmeester, C I Ratcliffe *Anal. Chim. Acta* **283** 1103 (1993)
183. P J Barrie, J Klinowski *Prog. Nucl. Magn. Reson. Spectrosc.* **24** 91 (1992)
184. D Raftery, L Reven, H Long, A Pines, P Tang, J A Reimer *J. Phys. Chem.* **97** 1649 (1993)
185. J Demarquay, J Fraissard *Chem. Phys. Lett.* **136** 314 (1987)
186. I V Koptyug, V B Fenelonov, L Yu Khitrina, R Z Sagdeev, V N Parmon *J. Phys. Chem. B* **102** 3090 (1998)
187. I V Koptyug, R Z Sagdeev, L Yu Khitrina, V N Parmon *Appl. Magn. Reson.* **18** 13 (2000)
188. I V Koptyug, S I Kabanikhin, K T Iskakov, V B Fenelonov, L Yu Khitrina, R Z Sagdeev, V N Parmon *Chem. Eng. Sci.* **55** 1559 (2000)
189. Y-Q Song *J. Magn. Reson.* **143** 397 (2000)
190. Y-Q Song *Magn. Reson. Imaging* **19** 417 (2001)
191. R Holly, H Peemoeller, C Choi, M M Pintar *J. Chem. Phys.* **108** 4183 (1998)
192. K J Packer *Prog. NMR Spectr.* **3** 87 (1967)
193. E W Hansen, R Schmidt, M Stocker, D Akporiaye *J. Phys. Chem.* **99** 4148 (1995)
194. R L Kleinberg, W E Kenyon, P P Mitra *J. Magn. Reson. A* **108** 206 (1994)
195. W E Kenyon, J A Kolleeny *J. Colloid Interface Sci.* **170** 502 (1995)
196. I Foley, S A Farooqui, R L Kleinberg *J. Magn. Reson. A* **123** 95 (1996)
197. R L Kleinberg, in *Encyclopedia of Nuclear Magnetic Resonance* Vol. 8 (Eds D M Grant, R K Harris) (Chichester: Wiley, 1996) p. 4960
198. K R Brownstein, C E Tarr *J. Magn. Reson.* **26** 17 (1977)
199. K R Brownstein, C E Tarr *Phys. Rev. A* **19** 2446 (1979)
200. S Chen, H-K Liaw, A T Watson *J. Appl. Phys.* **74** 1473 (1993)
201. S Davies, K J Packer *J. Appl. Phys.* **67** 3163 (1990)
202. S G Allen, P C L Stephenson, J H Strange *J. Chem. Phys.* **106** 7802 (1997)
203. E J Fordham, A Sezginer, L D Hall *J. Magn. Reson. A* **113** 139 (1995)
204. R L Kleinberg *Magn. Reson. Imaging* **12** 271 (1994)
205. J Godward, P Gunning, B P Hills *Appl. Magn. Reson.* **17** 537 (1999)
206. S P Roberts, P J McDonald, T Pritchard *J. Magn. Reson. A* **116** 189 (1995)
207. H-K Liaw, R Kulkarni, S Shen, A A Watson *AIChE J.* **42** 538 (1996)
208. K R McCall, D L Johnson, R A Guyer *Phys. Rev. B* **44** 7344 (1991)
209. S Davies, M Z Kalam, K J Packer, F O Zelaya *J. Appl. Phys.* **67** 3171 (1990)
210. M Peyron, G K Pierens, A J Lucas, L D Hall, R C Stewart *J. Magn. Reson. A* **118** 214 (1996)
211. P Fantazzini, C Garavaglia, G Guglielmi *Magn. Reson. Imaging* **19** 227 (2001)
212. G C Borgia, R J S Brown, P Fantazzini *J. Magn. Reson.* **132** 65 (1998)
213. G C Borgia, R J S Brown, P Fantazzini *J. Magn. Reson.* **147** 273 (2000)
214. E Almagor, G Belfort *J. Colloid Interface Sci.* **66** 146 (1978)
215. R K Cooper, J A Jackson *J. Magn. Reson.* **41** 400 (1980)
216. L J Burnett, J A Jackson *J. Magn. Reson.* **41** 406 (1980)
217. J A Jackson, L J Burnett, J F Harmon *J. Magn. Reson.* **41** 411 (1980)
218. R L Kleinberg, A Sezginer, D D Griffin, M Fukuhara *J. Magn. Reson.* **97** 466 (1992)
219. R L Kleinberg, C Flaum, in *Spatially Resolved Magnetic Resonance: Methods and Applications in Materials Science, Agriculture and Biomedicine* (Eds B Blümich, P Blümler, R Botto, E Fukushima) (Weinheim: Wiley-VCH, 1998)
220. K Overloop, L Van Gerven *J. Magn. Reson. A* **101** 179 (1993)
221. E W Hansen, E Tangstad, E Myrvold, T Myrstad *J. Phys. Chem. B* **101** 10709 (1997)
222. J H Strange, J B W Webber *Meas. Sci. Technol.* **8** 555 (1997)
223. J H Strange, J B W Webber *Appl. Magn. Reson.* **12** 231 (1997)
224. R Schmidt, E W Hansen, M Stocker, D Akporiaye, O H Ellestad *J. Am. Chem. Soc.* **117** 4049 (1995)
225. E W Hansen, R Schmidt, M Stocker *J. Phys. Chem. A* **100** 11396 (1996)
226. S G Allen, P C L Stephenson, J H Strange *J. Chem. Phys.* **108** 8195 (1998)
227. E W Hansen, M Stocker, R Schmidt *J. Phys. Chem. A* **100** 2195 (1996)
228. D Akporiaye, E W Hansen, R Schmidt, M Stocker *J. Phys. Chem. A* **98** 1926 (1994)
229. H F Booth, J H Strange *Mol. Phys.* **93** 263 (1998)
230. C Choi, B J Balcom, S D Beyea, T W Bremner, P E Grattan-Bellew, R L Armstrong *J. Appl. Phys.* **88** 3578 (2000)
231. P J Prado, B J Balcom, S D Beyea, T W Bremner, R L Armstrong, P E Grattan-Bellew *Cement Concrete Res.* **28** 261 (1998)
232. P J Prado, B J Balcom, S D Beyea, T W Bremner, R L Armstrong, R Pishe, P E Grattan-Bellew *J. Phys. D* **31** 2040 (1998)

[a] *Chem. Phys. Rep. (Engl. Transl.)*